The structure and dynamics of overturns in stably stratified homogeneous turbulence

By PETER J. DIAMESSIS[1]† AND KEIKO K. NOMURA[1]

[1]Department of Mechanical and Aerospace Engineering, University of California, San Diego,
La Jolla, CA 92093, USA

Direct numerical simulations of stably stratified homogeneous turbulence, with and without mean shear, are used to investigate the three-dimensional structure, evolution and energetic significance of density overturns. Although the flow conditions are idealized, examination of the full-field simulation data provides insight into flow energetics and mixing which may assist in the interpretation of physical measurements, typically limited to one-dimensional vertical profiles. Overturns, defined here through the density field as contiguous regions of non-zero Thorpe displacement, are initially generated by the stirring action of coherent vortex structures present in the flow and further develop through merging with adjacent overturns. During this growth phase, overturns exhibit irregular spatial structure in unsheared flow and elongated structure with distinct orientation in shear flow. Although most of the available potential energy (APE) and buoyancy flux are associated with stable (non-overturning) regions in the flow, young overturns actively contribute to the flow energetics. In particular, overturn peripheries are sites of high levels of APE, buoyancy flux and diapycnal mixing. A collapse phase may follow the growth phase in the absence of adequately strong mean shear. During this phase, buoyancy gradually assumes control of the overturns and their vertical scale steadily decreases. The energetic significance of the overturns diminishes, although high APE and diapycnal mixing continue to occur near their boundaries. In the final phase of their evolution, overturns contribute negligibly to the energetics. The remaining overturns are characterized by a viscous–buoyant balance which maintains their vertical scale. The overturns eventually vanish due to homogenization of their internal density distribution by diffusion. Activity diagrams, sampled at different points of flow evolution, show significant variation in overturn Reynolds and Froude numbers which may have implications for vertical sampling of a turbulent event.

1. Introduction

In stratified flows, overturns, i.e. regions where heavy fluid resides over light within the same fluid column, are often viewed as indicators of where the turbulence has overcome the stabilizing effect of the mean stratification and are thus considered active sites of stirring and mixing. They have been the focal point in the study of vertical transport and mixing in naturally stratified water bodies, particularly in oceanic microstructure studies. Typical microstructure measurements consist of

† Present address: Department of Aerospace and Mechanical Engineering, University of Southern California, Los Angeles, CA 90089-1191, USA.

localized vertical profiles of temperature and salinity in which overturns are identified as regions of non-zero Thorpe displacement, $d(z)$, defined as the distance a fluid particle is displaced when an observed density profile is rearranged to generate a gravitationally stable profile (Thorpe 1977). Since these regions are associated with mixing, they are used to estimate vertical diffusivities and energy dissipation rates. The lack of complete time and space information in these complex flows necessitates making assumptions which have led to variations in the interpretation of the measurements. For example, some consider overturns as young, actively turbulent events with high dissipation rates of turbulent kinetic energy and mixing (Gregg 1987; Hebert *et al.* 1992). An opposing school of thought (Gibson 1980, 1986, 1991) considers overturns to be remnants ('fossils') of previous rare but powerful turbulence, associated with negligible energy dissipation rates at the time of observation but significant diapycnal mixing induced by the fossilized patterns in the density field. In general, no concrete description exists of the three-dimensional structure and dynamical evolution of overturns because the available data are mainly limited to one-dimensional vertical profiles and single realizations of the events (Dillon 1984; Moum 1996).

Controlled laboratory experiments on stratified homogeneous turbulence, the simplest model for turbulence subject to stratification, can be used to provide a better understanding of overturns. The pioneering work of Van Atta and coworkers (Stillinger, Helland & Van Atta 1983; Itsweire 1984; Itsweire, Helland & Van Atta 1986; Rohr *et al.* 1988) was the first to experimentally study stratified homogeneous turbulence, with and without background shear. This series of laboratory studies recently culminated in the work of Keller & Van Atta (2000, hereafter referred to as KVA) who carried out experiments in a stratified homogeneous shear flow of air. Using an eight-point rake of temperature probes together with the frozen flow hypothesis, KVA constructed two-dimensional temperature fields. Based on their results, they proposed a generation mechanism of overturning based on vertical advection of fluid lumps. However, without information on the underlying velocity field, their description is inherently incomplete. High-resolution vertical temperature profiles were obtained using a new rapid traversing system. These were used to evaluate the Thorpe scale, $\langle L_T \rangle = \langle d(z)^2 \rangle^{1/2}$, which characterizes the vertical scale of overturns. The streamwise development of $\langle L_T \rangle$ was examined for a range of gradient Richardson numbers, Ri. For low Ri (weak stratification), $\langle L_T \rangle$ increases throughout the evolution, indicating that the size of overturns continues to increase. For high Ri, $\langle L_T \rangle$ initially increases, decays slightly, then remains roughly constant. This led KVA to deduce that, while the total energy of the flow continues to decay in the late stage of evolution, it is the number of overturns that diminishes and not their size. It was suggested that the minimum size could be related to a viscous cutoff; however this could not be verified through their data.

The vertical profiles were also used to examine the energetics of the flow in terms of the available potential energy, APE. The APE is defined as the excess of potential energy in the flow with respect to the background state of potential energy, BSPE, which is the state of minimum potential energy attained by the fluid if allowed to restratify adiabatically (Winters *et al.* 1995). In KVA, the BSPE was determined by reordering each individual profile, rather than a volume as may be done with full flow field data (see Appendix A). In this case, by definition, the APE is associated only with overturns ($d(z) \neq 0$). KVA find that the APE is much less than the turbulent potential energy, $PE \equiv 0.5 N^2 L_t^2$ (N is the buoyancy frequency and $L_t \equiv \langle \rho'^2 \rangle^{1/2}/\mathrm{d}\overline{\rho}/\mathrm{d}z$ is the Ellison scale, where $\langle \rho'^2 \rangle^{1/2}$ and $\mathrm{d}\overline{\rho}/\mathrm{d}z$ are the root-mean-square (r.m.s) value of the

density perturbations and the mean density gradient, respectively), suggesting that most of the temperature variance is associated with stable non-overturning regions. In fact, for homogeneous stratified turbulent flows, PE is the same as the APE of the flow (§4.2). The inaccurate evaluation of APE makes any deduction of the energetic significance of stable and unstable regions uncertain.

The diapycnal flux (molecular mixing across isopycnal surfaces) was also obtained using the background density from the reordered profiles. Although the experiments provide further insight into the vertical structure of the temperature field, the limitation of the measurements to vertical profiles and the lack of knowledge of the flow field leave an incomplete description of overturns and various outstanding issues: What is the three-dimensional spatial structure of overturns? What are the actual mechanisms of their generation and decay? Are overturns necessarily associated with the APE in the flow? What is their energetic significance and role in diapycnal mixing?

Direct numerical simulations (DNS) are advantageous as they provide detailed temporal and spatial information. There have been a number of DNS studies of homogeneous stratified turbulence. The majority of these studies have focused either on the overall energetics of the flow (e.g. Riley, Metcalf & Weissman 1981; Gerz, Schumann & Elghobashi 1989; Holt, Koseff & Ferziger 1992; Jacobitz, Sarkar & Van Atta 1997; Shih *et al.* 2000) or on small-scale structure and derivative quantities (Gerz, Howell & Mahrt 1994; Diamessis & Nomura 2000). The comparative evolution of average lengthscales of overturning has been examined by Metais & Herring (1989), Gerz & Schumann (1989*b*) and Itsweire *et al.* (1993). The latter study divided the evolution of the overall flow into different regimes based on the fossil turbulence theory of Gibson (1980, 1986, 1991). However, none of the above studies directly examined details of overturning events.

The objective of this work is to investigate overturns in stratified homogeneous turbulence, with and without shear, using DNS. The full field data provided by DNS is exploited to extract details of the structure and dynamic evolution of overturns. Such knowledge will provide a better understanding of the flow energetics and mixing and be useful in the interpretation of one-dimensional profile measurements. Although DNS is limited to relatively low Reynolds number flows, the shear flow conditions are comparable to that of KVA and the behaviours of the flows are in qualitative agreement. Issues arising from the work of KVA are addressed. The three-dimensional structure of overturns is educed by extending the one-dimensional Thorpe method to three dimensions and visualizing contiguous regions of non-zero Thorpe displacement. Examination of these structures and the underlyng flow field reveal the generation mechanism and subsequent evolution. The contribution and significance of overturns to the flow energetics and mixing are determined through conditional statistics and also by direct inspection of realizations of the flow. Although the overturn interiors do not make a major contribution to the overall flow TKE and APE budgets, the overturn peripheries are found to be active sites of APE, buoyancy flux and diapycnal mixing. Key dynamic processes occurring during the lifetime of the overturns are identified through the use of activity diagrams.

The simulations are described in §2. DNS results on overturn kinematics and dynamics are presented in §3 and §4. Further analysis and discussion are given in §5 and conclusions in §6.

2. Direct numerical simulations

DNS of homogeneous turbulence with uniform stable stratification and with and without a mean shear is performed for this study. The uniform mean vertical gradients

of the velocity $\boldsymbol{u}$ and density ρ are denoted by $S \equiv dU/dz$ and $d\overline{\rho}/dz$. The reference scales for velocity and density are $\Delta U = (dU/dz)L$ and $\Delta \rho = (d\overline{\rho}/dz)L$, where L is the height of the computational box. In the unsheared case, the reference velocity is the uniform mean velocity U. Relevant non-dimensional parameters include the turbulent Reynolds number based on the Taylor microscale, $Re_\lambda = v\lambda/\nu$, the Shear number, $Sh = Sv^2/\varepsilon$, and the Schmidt number, $Sc = \nu/D$. Here, v is the r.m.s turbulent velocity, ε is the kinetic energy dissipation rate, ν is the kinematic viscosity, and D is the mass diffusivity. The Taylor microscale is $\lambda = (15v^2\nu/\varepsilon)^{1/2}$. In these runs, density is solely determined by temperature. Thus, the Prandtl number, $Pr = \nu/\kappa$ (κ is the thermal diffusivity) can be used interchangeably with Sc. For the unsheared runs, the significance of the turbulence with respect to the mean stratification is given by the initial turbulent Froude number, $Fr = v/(l\,N)$, where $N = (-g\,d\overline{\rho}/dz/\,\rho_0)^{1/2}$ is the buoyancy frequency, $l = \pi \int (E(k,t=0)/k)dk/(2v^2)$ is the turbulent integral scale based on the initial isotropic turbulent energy spectrum $E(k,t=0)$ where k is the scalar wavenumber magnitude, and g is the acceleration due to gravity. For the sheared runs, the relative significance of stratification and mean shear effects is characterized by the gradient Richardson number, $Ri = N^2/S^2$. Finally, the buoyancy Reynolds number, $Re_b = \varepsilon/\nu N^2$, characterizes the separation of scales between the largest scale of turbulence not controlled by buoyancy and the smallest viscous scales (Ivey & Imberger 1991).

The governing equations describing the flow are the time-dependent continuity and Navier–Stokes equations with the Boussinesq approximation for the density. The numerical solution procedure is based on a second-order finite difference scheme in all three spatial directions with discrete Fourier interpolation for the mean advection term and second-order Adams–Bashforth time integration (Gerz *et al.* 1989). The computational domain is a finite cube containing 128^3 grid points. Periodic boundary conditions are employed in the x (streamwise) and y (spanwise) directions and shear-periodic conditions in the z (mean gradient) direction. The shear-periodic condition corresponds to continuous remapping by applying horizontal periodicity (see Gerz *et al.* 1989, for further details).

All simulations are initialized with the same fully developed isotropic turbulent velocity field and zero scalar (density) fluctuations. Such an initial configuration for the stratified simulations corresponds to a volume of turbulence upon which an unperturbed linear stratification is imposed with or without a uniform background shear. There is no initial lengthscale associated with the density field. This initial condition was first used by Jacobitz *et al.* (1997) primarily for the minimization of any nonlinear energy-transfer-induced transients observed in the initialization procedures of Holt *et al.* (1992) and Shih *et al.* (2000). Although the transients are minimized, they still occur because the turbulent velocity and density fields must become correlated and the turbulence must adjust to the background shear and stratification. Shear-induced transients may last up to time $St \approx 2.5$ (Jacobitz *et al.* 1997) which translates to $Nt \approx 1.76$ in the highest stratification runs of the present study. No observations or objective criteria exist to determine the exact duration of all other transients. In previous work, Diamessis & Nomura (1999) studied the effect of initial conditions on the structure and dynamics of gradient quantities in a stratified homogeneous shear flow; however, it is difficult to extrapolate the behaviour of overturns from such results. Thus, results of the present study should be interpreted keeping in mind the aforementioned transients. Note, however, that the present initial condition is particularly effective in allowing the identification of overturn generation mechanisms. The initially unperturbed neutrally or weakly stratified density field

Run	Re_λ	Sh	$Sc\ (Pr)$	Ri	Fr	Re_b
RUS1	20	0	0.7	–	1.86	117
RUS2	20	0	0.7	–	0.93	29
RUS3	20	0	0.7	–	0.58	12
RS1	20	3.2	0.7	0.05	1.86	117
RS2	20	3.2	0.7	0.2	0.93	29
RS3	20	3.2	0.7	0.5	0.58	11.7
RS4	20	3.2	0.7	1.0	0.41	5.9

TABLE 1. Simulation runs and associated initial non-dimensional parameter values.

provides the 'cleanest' configuration to observe the overturning effect of small-scale coherent flow structures (see §4.1). In such a situation, buoyancy does not control the scales of the flow structures and thus the overturn generation mechanism should be the same for either an unperturbed or an already stirred and mixed density field as in the initial condition of Holt *et al.* (1992) and Shih *et al.* (2000). For the most up-to-date discussion of initialization techniques of stratified turbulence simulations the reader is referred to Dommermuth *et al.* (2002).

A list of the simulations performed and the values of the associated parameters is given in table 1 (RUSx designates unsheared and RSx sheared runs). The initial values of Re_λ and Sh (for the sheared runs) as well as the value of Sc are kept fixed. The relative intensity of the initial isotropic turbulence velocity field with respect to the mean velocity, $(2E_k/3)^{1/2}/U$ (E_k is the turbulent kinetic energy, TKE) is equal to 0.0234 for all runs. The values of Fr, Ri and Re_b are varied by changing N. The choice of the specific values of Fr was dictated by the sheared runs, in which a critical (stationary) value of Ri, $Ri_{cr} \approx 0.1$, designates distinct flow regimes. Above Ri_{cr}, the growth of the TKE is inhibited by buoyancy forces (Holt *et al.* 1992; Jacobitz *et al.* 1997; Shih *et al.* 2000). Cases of subcritical, weakly supercritical and highly supercritical stratification with $Ri = 0.05$, 0.2 and 0.5, respectively, are thus considered. A sheared run of $Ri = 1$ was also performed (RS4). The results are similar to those of run RS3 but exhibit distinct net countergradient fluxes of momentum and mass not observed in any of the other runs. The aforementioned value of Ri_{cr} agrees with the $Ri_{cr} = 0.095$ of KVA but is lower than the theoretically predicted value of 0.25 due to the low Re_λ of the DNS (Jacobitz *et al.* 1997). The initial Sh was chosen to be within the range of values that allow the turbulence to grow by extraction of energy from the mean shear against viscous and linear effects (Jacobitz & Sarkar 1999). The low values of initial Re_λ and Pr are dictated by computational restrictions.

To ensure adequate grid resolution, the criterion $L_K k_{max} > 1$ was satisfied where $L_K = (\nu^3/\varepsilon)^{1/4}$ is the Kolmogorov lengthscale and k_{max} the maximum resolved wavenumber (Pope 2000). Computed energy and dissipation spectra indicate resolution of the dissipative scales of motion beyond the peak of the dissipation spectrum whereas no energy accumulation occurs at the highest resolved wavenumbers. Therefore, for the purpose of this present study, the above resolution criterion should be adequate despite the low-order finite difference scheme employed and any truncation-error-induced artificial dissipation. In addition, the two-point velocity correlation $R_{uu}(r_x)$ was evaluated as a suitable check for the validity of periodic boundary conditions in the x-direction (Nomura & Elghobashi 1992).
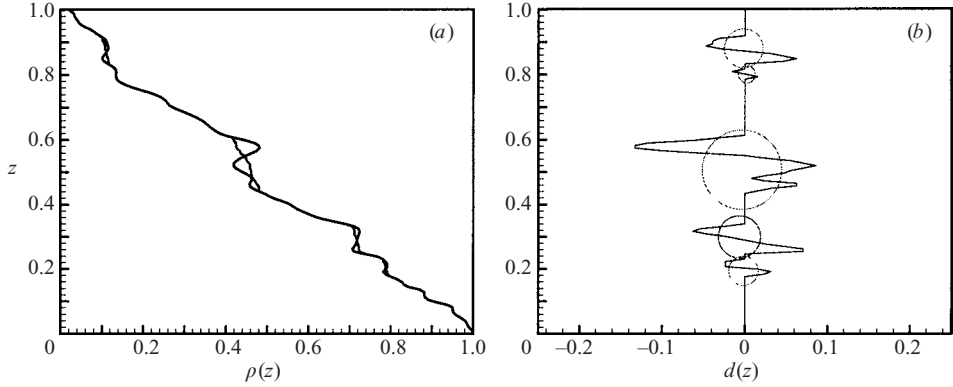
FIGURE 1. Thorpe-sorting of a sample vertical density profile $\rho(z)$ for $Ri = 0.05$ ($St = 2$): (a) Measured profile (solid line) with Thorpe-sorted profile (dotted line), (b) profile of displacement $d(z)$ (dotted circles delineate overturns).

Despite the computational limitations, the DNS flow conditions are comparable to those of KVA's wind-tunnel experiments. In KVA, the initial Re_λ is 30, $Sh \approx 3$, $Pr = 0.7$, and the range of Ri values considered is $Ri \in [0.015, 0.5]$.

3. Overturn kinematics
3.1. *Identification of three-dimensional overturns*

In the analysis of vertical density profile measurements, overturns are identified as regions of non-zero Thorpe displacement, $d(z)$, which is the distance a fluid parcel in the measured density profile is displaced during the sorting process that produces a gravitationally stable profile. Figure 1 shows a representative instantaneous $\rho(z)$ profile from the DNS data with the corresponding sorted profile and the profile of $d(z)$. The overturns correspond to segments of $d(z) \neq 0$ and exhibit a typical signature of a reverse Z-shape in the $d(z)$ profile (Dillon 1982; Itsweire 1984; KVA). The rare exception of $d(z) = 0$ in the interior of an overturn may occur in the core of such an event where the density field is homogenized due to molecular diffusion. Note that overturns contain both positive and negative $\partial\rho/\partial z$ although all $\partial\rho/\partial z > 0$ in the flow occur only within the interior of overturn regions. In addition, according to the definition of a complete overturn of Dillon (1984), the values of ρ inside a given overturn are not found anywhere else in the profile.

Hereafter, the term 'overturn segment' will denote a contiguous *one-dimensional* segment of a vertical profile associated with $d(z) \neq 0$, whereas 'overturn patch' refers to a contiguous *three-dimensional* region of $d(z) \neq 0$. Both structures have the characteristic property of consisting of heavy fluid over light. In the cases where the distinction between one-dimensional and three-dimensional structure is not necessary, the term 'overturn' is simply used. It is emphasized that in this work overturns are educed using information from the structure of the density field alone. The associated velocity or vorticity fields are not taken into account in the definition.

3.2. *Spatial structure and intermittency of three-dimensional overturns*

The three-dimensional structure of overturns is examined by visualizing overturn boundaries, i.e. the spatial envelope of $d(z) \neq 0$. As in subsequent sections, the focus here is on runs of moderate to high stratification (RS2, RUS2 and RS3). Note that
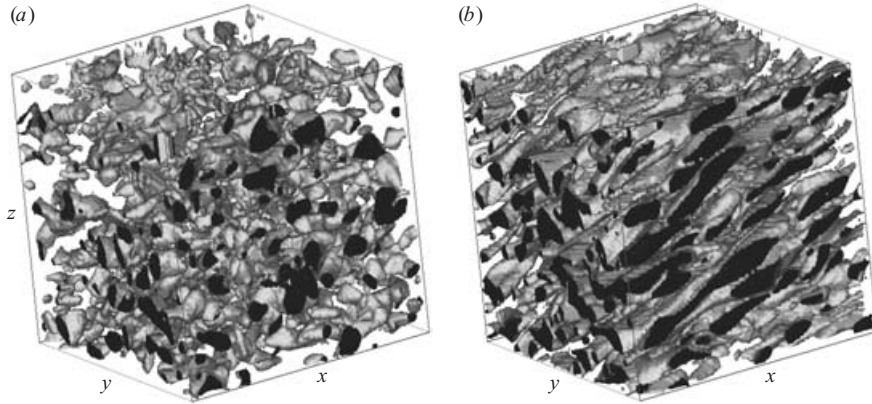
FIGURE 2. Overturn boundaries (spatial envelope of non-zero Thorpe displacement) over the entire computational domain, at $Nt = 0.9$ ($St = 2$): (a) Run RUS2, and (b) Run RS2.

visualizations of cases RS1 and RUS1 have been omitted as the high volume fraction of overturns renders the discernment of any individual overturning events extremely difficult. Plane-cuts across the flow field indicate that the overturns are much larger in both the vertical and horizontal directions, with the qualitative nature of these structures being similar to that in runs RS2 and RUS2.

Figure 2 illustrates the spatial structure of overturns in runs RUS2 and RS2. By $Nt = 0.9$ ($St = 2$) a striking difference is observed. While in the unsheared flow RUS2 (figure 2a), the overturns are irregular structures with a random orientation, in the sheared flow RS2 (figure 2b) they exhibit a characteristic elongated structure inclined from the horizontal plane. These features are due to the preferential orientation of the vortical structures that generate the overturns (see §4.1) and advection by the mean shear. The above difference may be contrasted with the similar initial evolution ($Nt < 2$) of the overturn lengthscale in both of these runs (see §3.4).

Figure 3 show overturns at various times for case RS3 to illustrate the growth and subsequent gravitational collapse of the overturn events for a high value of N. Figure 3(a) shows significant overturns having been generated at small scales by $Nt = 0.71$ (see also §3.4). The overturns begin to approach their maximum size by time $Nt = 1.42$ (figure 3b) while the distinct structure and directional preference caused by the shear are quite evident. The size and number of overturns have diminished by $Nt = 4.26$ (figure 3c). The overturn population continues to diminish, yet its vertical extent remains relatively constant as seen in figure 3d at time $Nt = 5.68$ (also demonstrated in figure 7). Evidently, certain overturns survive longer than others. Animations (not shown here) confirm that these events are older patches in the process of arrested collapse and not newly generated overturns. The structure of overturns for run RUS3 is considered in detail in Diamessis (2001) and its only difference with run RS3 is the absence of shear effects in the patch structure, as in the comparison between runs RUS2 and RS2.

Figure 4 shows (x, z) and (y, z) plane-view cuts of the overturn boundaries superimposed on isopycnals for run RS2 at time $Nt = 2.68$. Some noteworthy features of the density field associated with the overturns may be observed. In figure 4(a), a distinct orientation from the streamwise direction is evident. As observed by KVA, the strongest $\nabla\rho$ is negative (stable due to the stable mean gradient) and here it is seen to occur just outside the boundaries of the overturns, often between two overturning events. The upward slope of sheets of high magnitude $\nabla\rho$ (figure 4a) can be attributed
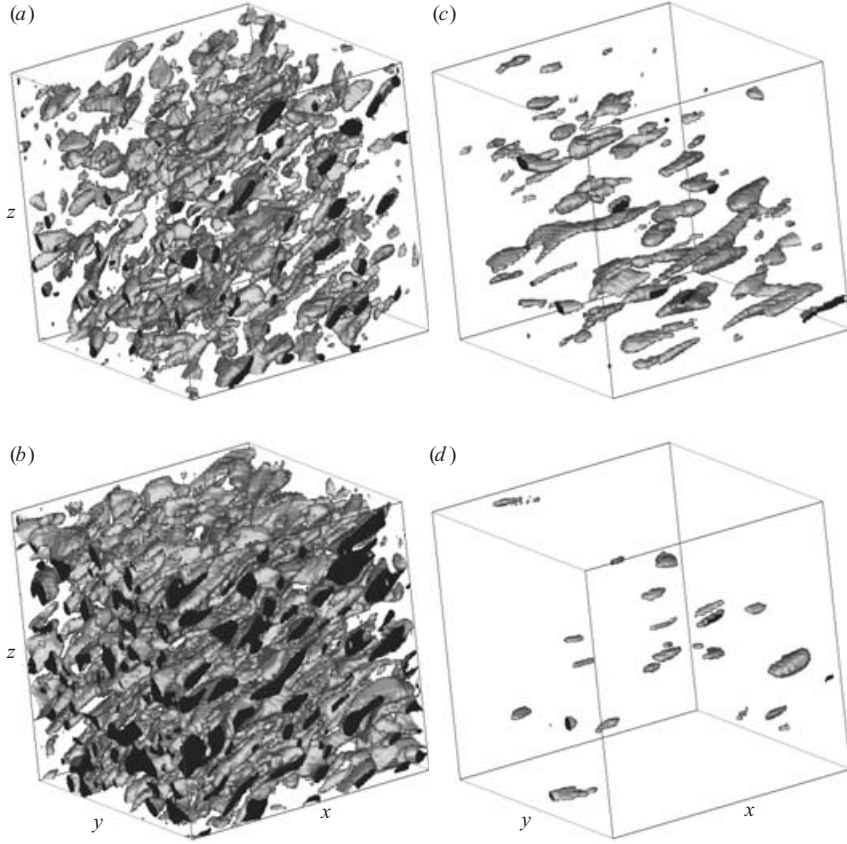
FIGURE 3. Overturn boundaries (spatial envelope of non-zero Thorpe displacement) in the entire computational domain for run RS3: (*a*) $Nt = 0.71$, (*b*) 1.42, (*c*) 4.26, (*d*) 5.68.
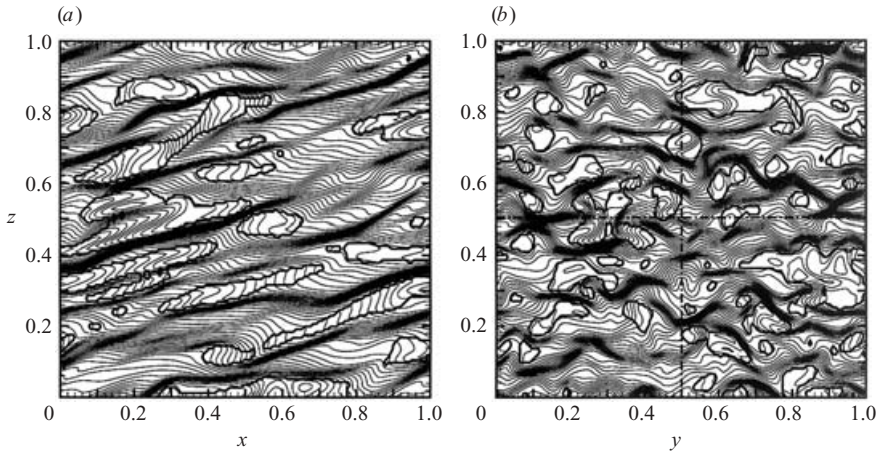

FIGURE 4. Plane-view cuts across the flow for sheared run RS2 ($Nt = 2.68$. Thick lines represent overturn boundaries and thin lines are isopycnals. (*a*) (x, z)-plane at $y = 0.15625$ and (*b*) (y, z)-plane at $x = 0.16$. the dash-dotted lines in (*b*) divide the plane into four quadrants. The bottom left one is the focus of visualizations used in §4.2.
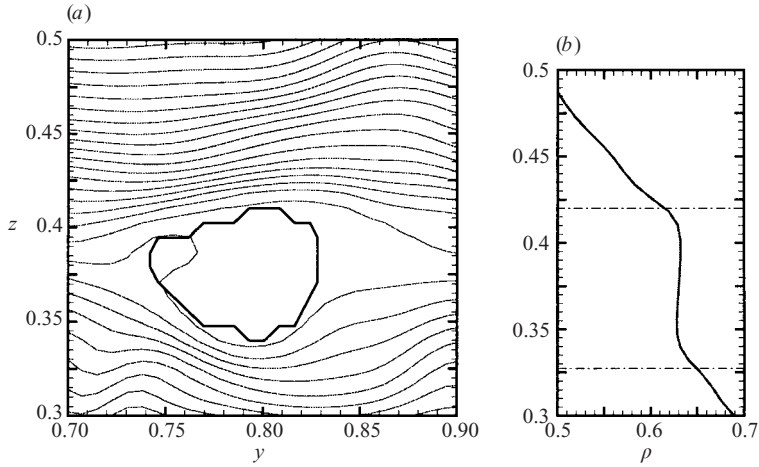
FIGURE 5. (*a*) Close-up of plane-view cut across the flow ((y, z)-plane at $x = 0.97$) for run RS3 ($Nt = 5.68$). Thick lines represent overturn boundaries and thin lines are isopycnals. (*b*) Vertical density profile across the centre of a specific overturn.
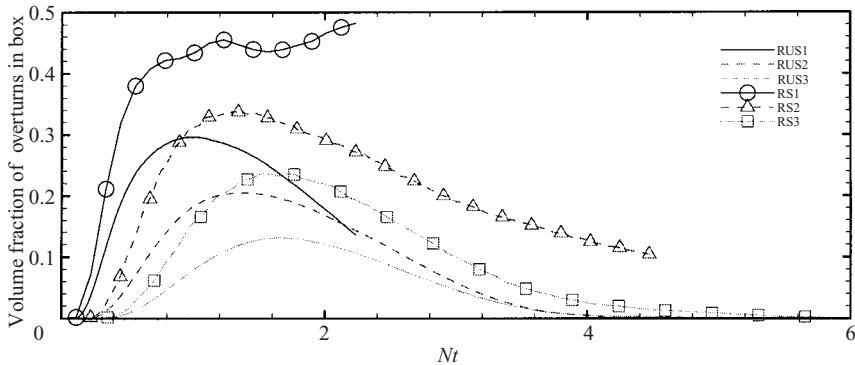

FIGURE 6. Time development of the fraction of the flow volume occupied by overturns.

to the preferential orientation of compressive strain in the shear flow (Nomura & Diamessis 2000; Diamessis & Nomura 2000). Figure 5 illustrates a close-up of a (y, z) plane-view cut across a typical overturn at a later time $Nt = 5.68$ for run RS3, along with a vertical density profile extracted from the centre of the illustrated overturn. A homogenous density distribution within the overturn with a slightly positive value of $\partial\rho/\partial z$ is observed. Note that run RUS2 exhibits qualitatively similar features to run RS2 but without the directional preference due to shear (see Diamessis 2001, for more details).

A measure of the spatial intermittency of overturns is the volume fraction of the flow occupied by them. The evolution of this quantity is shown in figure 6. In the unsheared flows, the volume fraction initially grows. Lower values of maximum volume fraction are observed at higher N (run RUS3). This maximum value is attained in the interval $1 < Nt < 2$. The high-stratification runs (supercritical: $Ri > Ri_{cr}$) for the sheared flows exhibit similar behaviour to the unsheared flows, the main difference being that the maximum volume fraction value is higher and the rate of decrease is slower for the sheared cases. In run RS1 (subcritical: $Ri < Ri_{cr}$), shear continues to supply energy to

the turbulence. Thus, the overturns grow to occupy about 50% of the flow volume by the end of the simulation. It is interesting to compare this number to the observation of Saggio & Imberger (2001) who found on the average that the energetic central metalimnion (thermocline) of a lake, dominated by $Ri < 0.5$, has 35% of its volume occupied by overturns.

3.3. *Overturn lengthscale definition*

As indicated in §1, a measure of the vertical scale of the overturning motion within a greater turbulent region is given by the average Thorpe scale $\langle L_T \rangle$. If all N_P available vertical density profiles containing overturns are sorted into stable ones, then

$$\langle L_T \rangle = \left[\frac{1}{N_P} \sum_{i=1}^{N_P} L_{T_i} \right]_{L_{T_i} \neq 0}. \tag{3.1}$$

In the present DNS results, $\langle L_T \rangle$ describes the *average overturning length* over the entire flow. L_{T_i} is the average Thorpe scale of an individual profile, defined as

$$L_{T_i} = \left[\frac{1}{M} \sum_{j=1}^{M} d(z_j)^2 \right]_{d(z_j) \neq 0}^{1/2}, \tag{3.2}$$

where $d(z_j)$ is the Thorpe displacement and M is the number of points in the profile with $d(z_j) \neq 0$. Note that $\langle L_T \rangle$, as defined by (3.1) and (3.2), differs from that of other DNS studies (Itsweire *et al.* 1993; Smyth & Moum 2000). In contrast to these studies, only profiles containing points with $d(z_j) \neq 0$ are taken into account. This is consistent with the common oceanographic practice which recognizes that the most accurate estimate of the average height of overturning in the water column is obtained when one employs only profiles with non-zero Thorpe displacements (Moum 1996; Smyth, Moum & Caldwell 2001). The same methodology was used by KVA who sampled 300 to 500 profiles at each individual measurement location. As shown later on, the above difference in methodologies can lead to disagreements in the interpretation of the evolution of overturning events, particularly in the final stages of their evolution (see §3.4). A related lengthscale is the average maximum Thorpe scale, $\langle L_{Tmax} \rangle$, which is the average over all available profiles of the maximum Thorpe displacement of each profile (see Itsweire *et al.* 1993). Consistent with $\langle L_T \rangle$, $\langle L_{Tmax} \rangle$ takes into account only profiles containing instabilities. This lengthscale serves as a measure of the vertical scale of the largest events within the flow's overturn population. In all runs considered here, the ratio $\langle L_{Tmax} \rangle / \langle L_T \rangle$ ranged from 2.5 to 1, depending on the degree of stratification and the spatial intermittency of the overturning patches, i.e. the further $\langle L_{Tmax} \rangle / \langle L_T \rangle$ departs from a value of 1, the greater the range of overturns of different scales (from small to largest) present in the flow (Smyth & Moum 2000).

3.4. *Overturn lengthscale evolution*

The evolution of $\langle L_T \rangle$ is shown in figure 7(*a*). Runs RUS1 and RS1 have a similar initial evolution until $Nt \approx 1$. At that point, RUS1 exhibits a decay. RS1, however, exhibits a short period of zero growth rate succeeded by a constant increase as the turbulence enters its asymptotic phase of shear-driven exponential growth. Runs RUS2 and RS2 exhibit a similar initial growth until time $Nt \approx 1$ after which a slower rate of decay is observed in the (weakly supercritical) sheared case. The strong-stratification runs (RUS3, RS3) exhibit the same behaviour regardless of the presence of shear. $\langle L_T \rangle$ grows until $Nt \approx 2$ and then decreases by a factor of two by $Nt \approx 4$.
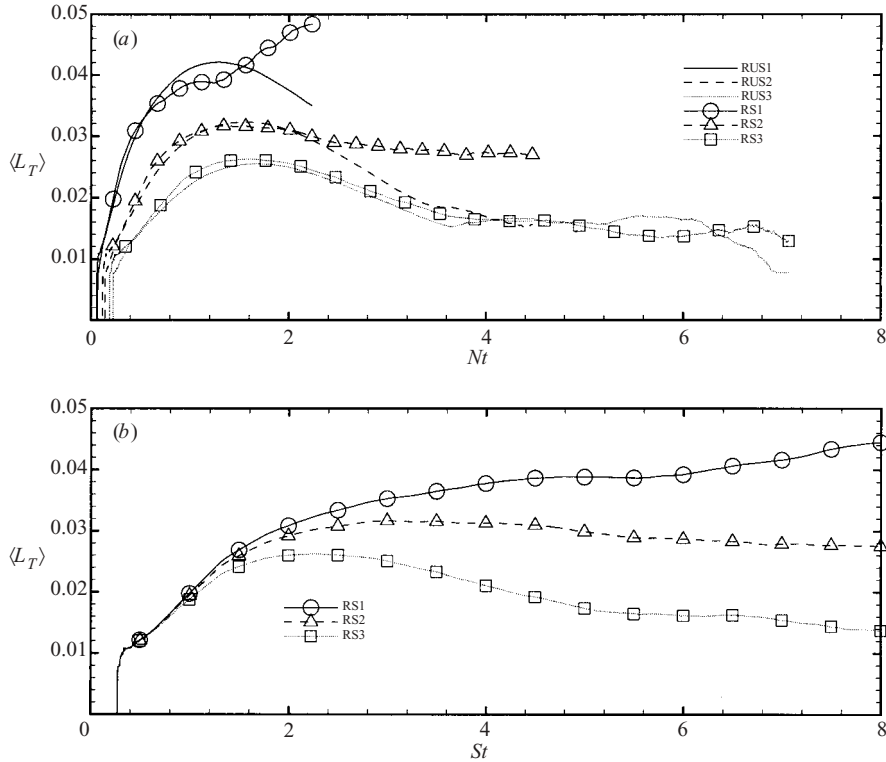
FIGURE 7. Time series of average Thorpe scale $\langle L_T \rangle$: (a) unsheared and sheared runs, time scaled with N, (b) sheared runs, time scaled with S.

It then remains constant until $Nt \approx 7$. The fact that $\langle L_T \rangle$ remains constant while the corresponding overturn flow fraction volume drops rapidly (figure 6) indicates that there are progressively fewer overturns of a relatively constant size. Such a behaviour of the overturn population was extrapolated by KVA from a comparison of $\langle L_T \rangle$ with the overturn (Ellison) lengthscale L_t (defined in §1). If one had used the definition of $\langle L_T \rangle$ of Itsweire *et al.* (1993) and Smyth & Moum (2000) (which includes all profiles in the dataset under consideration, see §3.3), the spatial intermittency of overturning events would have been averaged out and $\langle L_T \rangle$ would instead exhibit a rapid decrease to zero. In addition, the ratio of $\langle L_T \rangle$, calculated through these two different definitions, to L_t (not shown here) is found to behave exactly as in figure 17 of KVA. $\langle L_T \rangle$ as defined in (3.1) and (3.2) does not behave proportionally to L_t throughout the flow evolution, particularly in the late phases of the strongly stratified runs, where $\langle L_T \rangle$ is small and L_t is controlled by significant wave-like disturbances present in the flow (Smyth & Moum 2000). Thus, the use of L_t is not warranted when characterizing *overturn event geometry*.

Finally, if one plots the evolution of $\langle L_T \rangle$ for the sheared runs with time scaled by S (figure 7b) the behaviour observed is qualitatively consistent with that shown in figure 16 of KVA. It is of interest to note that at early times, all four sheared runs exhibit an identical, Ri-independent growth from a zero value. Similar observations were made for the corresponding results from the unsheared runs (not shown), when time was scaled with the initial large-eddy turnover time. Although this early growth behaviour occurs partly during the initialization-related transients, these observations
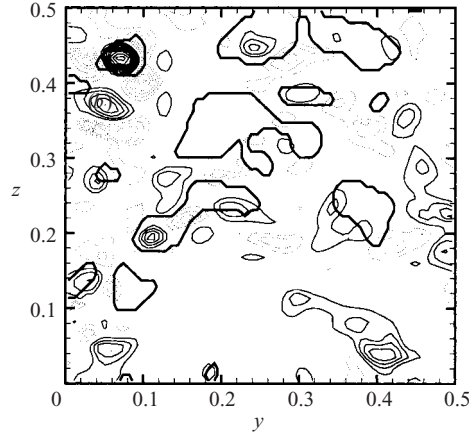
FIGURE 8. Plane-view cut across a 64^3 subdomain of flow RS2, at time $Nt = 2.68$ (y, z)-plane at $x = 0.16$, showing overturn boundaries (thick solid lines) and contours of the second invariant of the velocity gradient tensor $II = w^2/2 - S^2$, normalized by the average enstrophy of the flow $\langle w^2 \rangle$. Contour value spacing is 0.1; thin sold lines: positive values (minimum and maximum values 0.1 and 1, respectively), thin dotted lines: negative values (minimum and maximum values -1 and -0.1, respectively). Overturns associated with high II are young events undergoing active turbulent stirring.

suggest that the overturn generation mechanism is stratification-independent, given the identical initial velocity fields of the sheared runs (and those of the unsheared runs). This possibility is discussed in greater detail in §4.1.

4. Overturn dynamics

4.1. *Overturn generation mechanisms*

As indicated by figure 7(b), the generation mechanism of overturns is independent of stratification. Given the initial passive scalar nature of the density (due to the small early displacements of the isopycnals and the weak restoring buoyancy forces), the initial growth of $\langle L_T \rangle$ should be independent of any transients associated with the adjustment of the initially unperturbed density field to the turbulence. In addition, the limited separation of lengthscales (as indicated by the low Re_b) suggests that overturns are likely to be generated by small-scale motion in the flow. Previous DNS with a linear density profile $(\mathrm{d}\overline{\rho}/\mathrm{d}z < 0)$ in zero gravity (Diamessis & Nomura 2000) revealed that regions of strong positive fluctuating vertical density gradient, $\partial \rho'/\partial z > 0$, a condition always associated with overturning, are largely associated with regions of high-amplitude vorticity ω and low-amplitude strain rate, $\mathbf{S}$, i.e. high positive value of the second invariant of the velocity gradient tensor, $II = \omega^2/2 - \mathbf{S}^2$, which are known to form tube-like vortex structures (Nomura & Post 1998; Diamessis & Nomura 2000). Evidence of the association of young overturns and high $II > 0$ regions is given in figure 8, which shows a (y, z) quarter-plane snapshot corresponding to the lower-left quarter-plane in figure 4(b) (i.e. at time $Nt = 2.68$ for run RS2). The plot shows overturn boundaries overlaid on contours of II. At this time, the flow contains a collection of older (in some cases collapsing) overturns and relatively younger ones. Overturns coinciding with regions of high-amplitude $II > 0$ are generally found to be smaller in size and thus considered young active events. Figure 9(a) shows a close-up view of a typical young overturn and illustrates the stirring/overturning
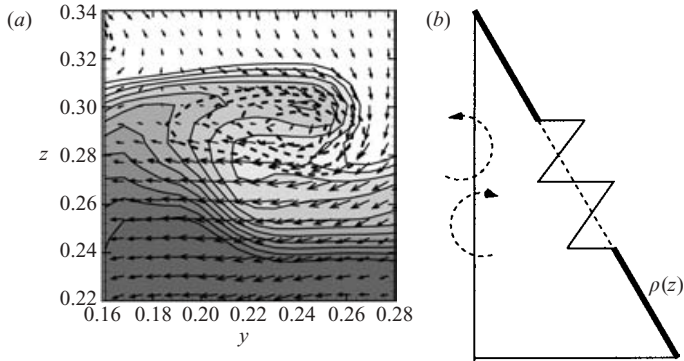
FIGURE 9. (*a*) Close-up view of small-scale overturning event in the (y, z)-plane at $x = 0.25$ for $Ri = 0.05$ flow ($St = 2$), showing isopycnals with the corresponding velocity field. Dashed lines are contours of streamwise vorticity. (*b*) Illustration of the effect of vortex structures on a linear density profile.

action of the vortex tubes. Superimposed on the density field are velocity vectors and dashed contours of streamwise vorticity which indicate the presence of a vortex of elliptical cross-section. The vortex instigates overturning by wrapping the isopycnals around its core and rapidly entrains ambient fluid. The strong $\nabla \rho$ observed at the overturn boundary is associated with the strong compressive strain occurring at the periphery of the vortex, the structure of which bears similarities to the Burgers vortex (Nomura & Post 1998).

In the presence of mean shear, the vortex structures tend to exhibit distinct spatial orientation (Nomura & Diamessis 2000). As observed in figure 2(*b*), the preferred orientation of these structures is imparted to the generated overturns which further develop in the presence of mean shear. The effectiveness of the vortex structures in causing overturning is enhanced by background shear, which promotes horizontal ω by amplification of the perturbation vorticity at first in the streamwise and later in the spanwise direction (Nomura & Diamessis 2000). Strong horizontal vorticity establishes $\partial \rho' / \partial z > 0$ through rotation of the imposed mean stratification (Diamessis & Nomura 2000). In the unsheared flow, where the turbulence is initially isotropic, the vortex tubes have no specific directional preference and thus their ability to overturn is not optimally exploited. A similar statement can be made for sheared flows with high values of the ratio Re_λ / Sh, which are associated with a more isotropic orientation of the vortex tubes (Nomura & Diamessis 2000).

Figure 9(*b*) depicts the stirring action of the vortices by showing the effect of two counter-rotating horizontal vortices on a linear density profile. A disturbance of the density field by solid-body rotation generates initially a region of $\partial \rho / \partial z > 0$ with high $|\partial \rho / \partial z|^2$ at the boundaries. An adjacent counter-rotating vortex, acting either simultaneously or successively, can significantly enhance isopycnal compressive straining at overturn boundaries resulting in even stronger $\nabla \rho$ as illustrated in figure 9(*b*) and also in figure 4. The close proximity of such adjacent overturns allows them to merge and gradually establish a single contiguous region of $d(z) \neq 0$. This is how larger-scale overturns develop in the present flows. It is emphasized that this merging process refers strictly to the local development of the density field and not to the overturn-generating vortices.

Based on two-dimensional rake visualizations of their temperature data, KVA conjectured that overturns are generated by the localized vertical advection of well-mixed

lumps of fluid past their equilibrium position and subsequent displacement of stable
density fronts. A lump which is hotter (colder) than the ambient fluid produces an
overturned region above (below) it. This scenario may indeed be possible after the
density field has been sufficiently stirred and mixed. The present results indicate
that the vertical advection is associated with strong vortical structures in the flow.
Well-mixed lumps of fluid in the vicinity of a vortex may be formed through the
zero-gradient-point (hot and cold spot) production mechanisms as demonstrated in
the two-dimensional DNS of Gibson, Ashurst & Kerstein (1988). In the case of
the present three-dimensional DNS, the formation of such a zero-gradient point is
evidenced in figure 9(a) at the location $(y, z) \approx (0.24, 0.3)$.

4.2. *Contribution of overturns to energy budgets*

The energetic significance of overturns may be assessed by examining the contribution
of overturns to the budgets of TKE and APE. The budget equations and associated
quantities are described in Appendix A. Figures 10–15 show the time development of
the budget quantities (TKE, turbulence production, TKE dissipation rate, buoyancy
flux, APE and diapycnal flux) and compare the contribution of the overturns to
the total flow (volume integrated) value of each quantity. Included in these figures
are instantaneous realizations (y, z quarter-plane snapshots corresponding to the
lower-left quarter-plane in figure 4b) showing the spatial distribution of the energetic
quantities together with the location of the overturning patches. The selected time of
the snapshots provides a representative description of the flow conditions in which
there exists a significant range of overturning scales not controlled by buoyancy (i.e.
$Fr_S > Fr_S^{cr}$ as indicated in §5.1 despite the near constant value of $\langle L_T \rangle$ in figure 7b). As
illustrated in figure 8 and discussed in §4.1, at this time, the flow contains a collection
of both young and old overturns. The presentation is limited to the shear flow results
as the unsheared runs exhibit only quantitative differences (with the exception of
shear production P, which is zero by definition). In general, the sheared overturns
are characterized by much greater values of the TKE and APE budget quantities.
Note also that the $Ri = 0.05$ case (RS1) is not examined here due to the high fraction
of flow volume occupied by the overturns which makes it hard to isolate them as a
subset of the total flow with certain unique features.

Figure 10(a) shows the TKE ((A 1) in Appendix A) evaluated for the total flow as
well as the volume occupied by overturns for the three supercritical Ri simulations. The
total flow TKE exhibits a decay in all three cases. The TKE of the overturns grows
to a maximum within the interval $1 < Nt < 2$, following an evolution parallel to that
of the corresponding overturn volume fraction (figure 6). The TKE in the interior of
the overturns does not exceed more than approximately 40% of the total flow TKE.
When the overturns occupy more than 5% of the flow volume, the per-unit-volume
values of the TKE of these events (not shown) exhibit a 10% to 25% greater value
than their respective values in non-overturning regions. The difference is not large
enough to consider most TKE to be concentrated in overturning events. The TKE
within the overturns essentially grows proportionally to their volume fraction and
thus the TKE in the flow can be linked mostly to non-overturning motions. When
buoyancy begins to control the overturns, their volume fraction decreases along with
their TKE content, as they are less associated with turbulent stirring. In cases RS3
and RS4, at later times, the kinetic energy of the flow is associated with some form of
decayed turbulence. Further analysis would be required to determine the exact nature
of these residual motions and particularly what percentage of the associated kinetic
energy is contained in internal wave motions. Figure 10(b) shows contours of TKE
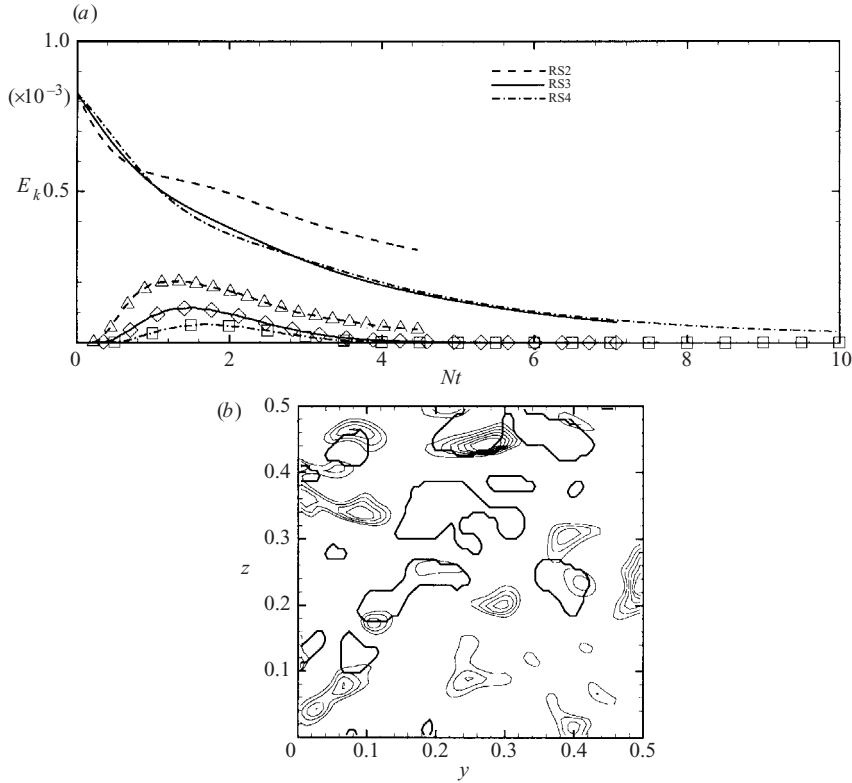
FIGURE 10. (*a*) TKE evaluated for the total flow (plain lines) compared to that for the volume occupied by overturns (lines with symbols), for sheared runs. (*b*) Plane-view cut across a 64^3 subdomain of flow RS2, at time $Nt = 2.68$ (y, z-plane at $x = 0.16$), showing overturn boundaries (thick solid lines) and contours of local value of TKE normalized by its spatial average. Minimum and maximum contour values are 3 and 8, respectively and contour value separation is 1.

and overturn boundaries for run RS2 at $Nt = 2.68$. Incidences of high TKE in the vicinity of overturn boundaries are occasionally observed and tend to be associated with younger overturns (figure 8).

The corresponding set of plots for the turbulence production P (A 2) is shown in figure 11. Maximum P for the total flow occurs at $Nt = 1$, with contributions from the overturning regions never exceeding 25%. The fraction of P associated with the overturns appears to follow their volume fraction. The per-unit-volume value of P for the total flow and overturns (not shown) exhibit similar behaviour to that observed for the TKE. In addition, the negative total flow turbulence production observed in runs RS3 and RS4 (see Holt *et al.* (1992) for an explanation of this phenomenon, which is considered to be transfer of energy back to the mean flow) appears not to be associated with any overturning activity, as P integrated over overturns exhibits a strict lower bound of zero. When examining the corresponding contour plot (figure 11*b*), high positive $-Su'w'$ occurs predominantly outside overturns. The few cases where high positive $-Su'w'$ is observed within overturns or at their boundaries are usually situations where the turbulence is actively stirring the density field (figure 8) and $-Su'w'$ is characterized by a dipolar structure (local maximum adjacent to a local minimum).
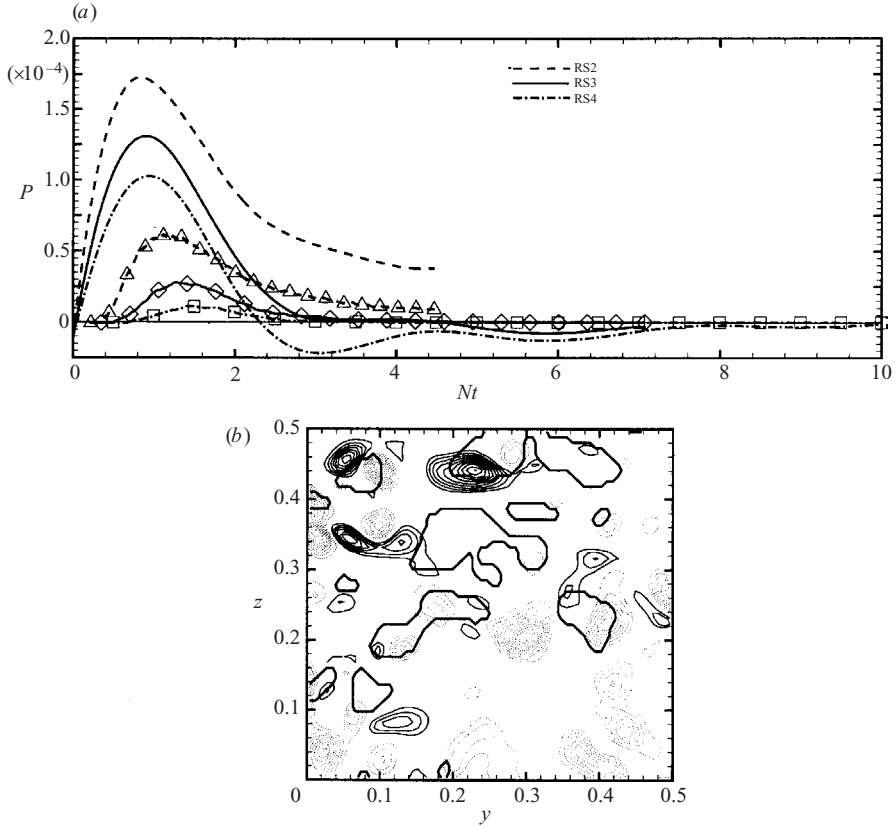
FIGURE 11. As figure 10 but for turbulence production P. (*b*) Overturn boundaries (thick solid lines) and contours of the local value of $-Su'w'$ normalized by its spatial average (solid lines: positive values, dotted lines: negative values). Contour values are in the range $[\pm 3, \pm 23]$, with separation 4.

The contribution of overturns to the buoyancy flux, Φ_z (A 2) is considered in figure 12. As seen in the associated time series, Φ_z is primarily associated with non-overturning motion, the contribution from overturning events decreasing with increasing Ri. The per-unit-volume value of Φ_z is approximately the same for both overturning and non-overturning regions. Similar to the case of negative production, negative Φ_z, which corresponds to restratification at high N (e.g. run RS4), is not associated with motions in the overturn interiors. However, Diamessis (2001) found that the periphery of a tracked individual three-dimensional overturning patch during collapse was characterized by non-negligible $\Phi_z < 0$. Further investigation is required to quantify the exact contribution of overturns to negative P and Φ_z. The corresponding contour plot for buoyancy flux (figure 12*b*) reveals that high $w'\rho'$ develops mostly outside overturns, yet strong positive buoyancy flux does occur at the boundaries of actively stirred overturns. This phenomenon is evidently associated with fluid being advected away from its equilibrium position, but not to the point where a heavy over light configuration has been established. Regions of positive Φ_z are observed to be accompanied by negative Φ_z in a dipolar configuration at the boundaries of overturns. This configuration as well as the similar one observed for P are associated with wrapping of the isopycnal surfaces around the core of the stirring
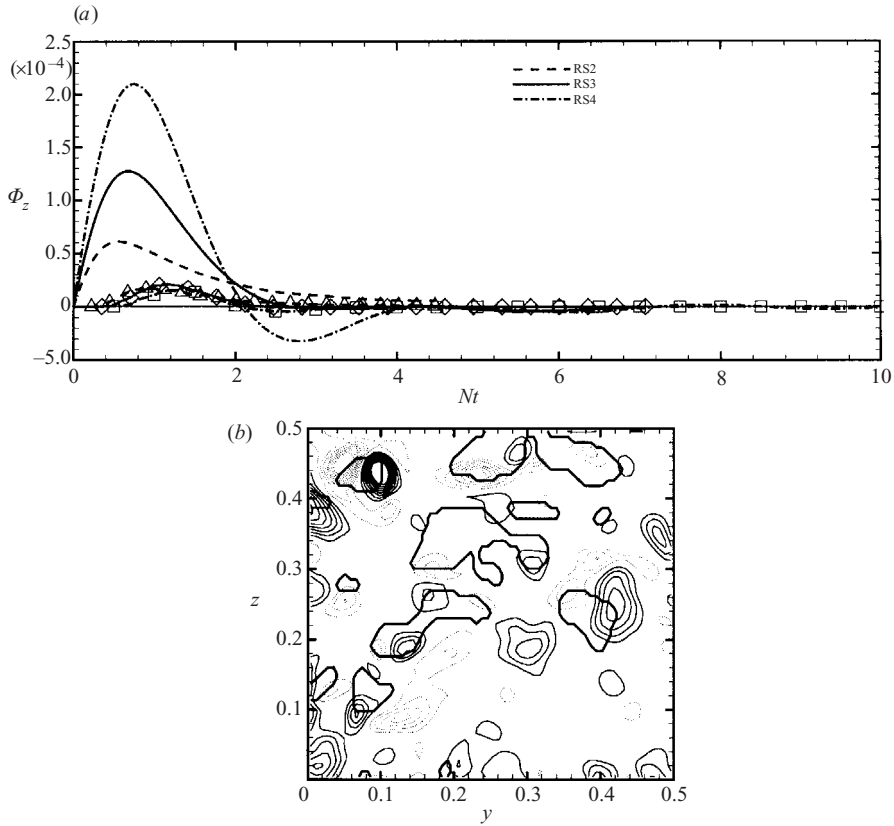
FIGURE 12. As figure 10 but for buoyancy flux Φ_z. (*b*) Overturn boundaries (thick solid lines) and contours of local value of $w'\rho'$ normalized by its spatial average (solid lines: positive values, dotted lines: negative values). Contour values are in the range $[\pm 2, \pm 16]$ with separation 1.

vortex. Finally, the strong restratification effects displayed by run RS4 for $Nt > 2$ (figure 12*a*) are not associated with collapsing overturning events as these occupy a negligible fraction of the flow volume.

The contribution of overturns to the TKE dissipation rate ε (A 2) is shown in figure 13. As indicated by the time series in figure 13(*a*), the overturns contribute little to the overall value of ε. Again, the contribution to ε of the overturn interior follows that of their flow volume fraction and the associated per-unit-volume value is the same as that of the non-overturning regions. Figure 13(*b*) suggests that strong dissipation rates do not tend to occur inside the overturns. Previous studies have shown that high ε (Diamessis & Nomura 2000) is associated predominantly with sheet-like structures characterized by comparable rotation and strain, which do not directly cause overturning (Diamessis 2001). However, high ε also occurs in sheets surrounding vortex tubes near the boundaries of certain overturns, which are associated with active stirring.

As expected, overturns play a more important role in establishing the APE of the flow as well as diapycnal mixing. The contribution of overturns to the APE (A 3) is shown in figure 14. The APE of the total flow and of the overturns reach a maximum value at time $Nt \approx 2$ for all cases, and then begin to decay. This result is consistent with the behaviour observed in figure 7(*a*) where the average overturn size, and thus
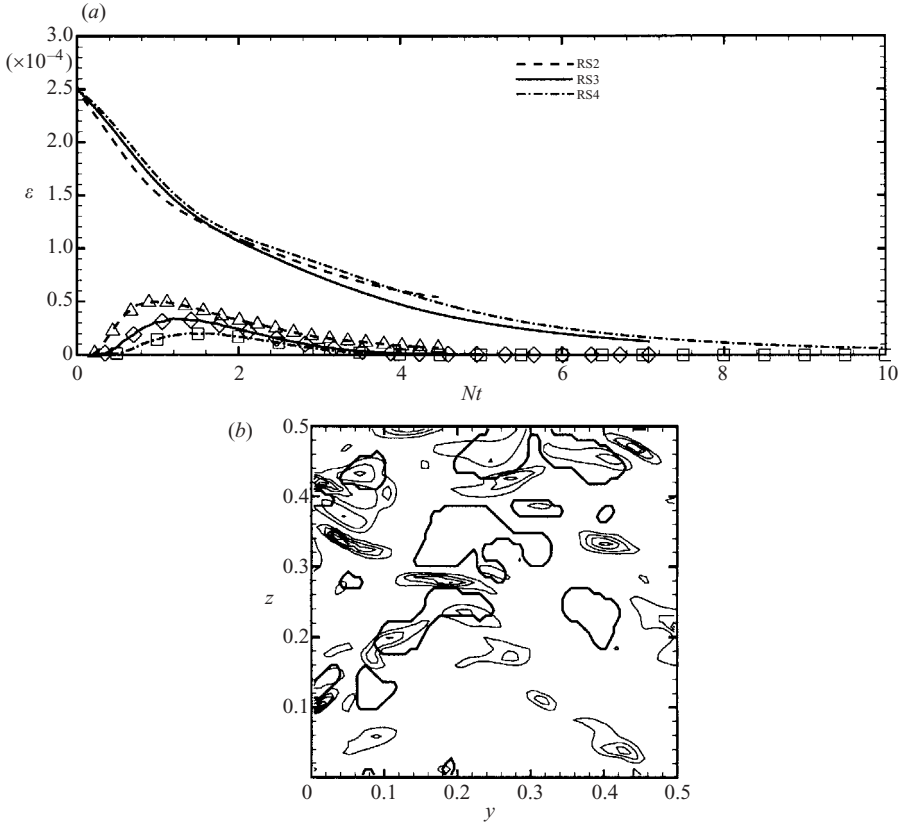
FIGURE 13. As figure 10 but for turbulent kinetic energy dissipation rate ε. (b) Overturn boundaries (thick solid lines) and contours of local value of ε normalized by its spatial average (solid lines). Contour values are in the range [1.5, 6.5] with separation 1.

a fluid parcel's displacement (APE), reaches a maximum at the same time and then begins to decrease due to gravitational collapse as the parcel's APE is converted back into kinetic energy. Note that the overturns never contribute more than 40% of the overall flow APE (and typically less), their contribution diminishing with time. This finding can be compared with results of KVA. As discussed in §1, KVA estimate APE using BSPE obtained from sorting the individual profile and thus their APE is associated only with overturns, although not precisely equal to the total APE of the overturns. They find the ratio APE/PE never exceeds 15% in the supercritical-Ri flows. In homogeneous stratified flow, the turbulent potential energy (see §1) $PE = 0.5L_t^2 N^2$, is the actual APE of the flow (Gerz & Schumann 1989a). Although not precise, the low value of APE/PE in KVA is consistent with the present results indicating that overturns are not the dominant contributor of the true flow APE. Nevertheless, the overturns do contribute in establishing APE. Figure 14(b) reveals that high APE tends to exist in the immediate vicinity of overturn boundaries. As in the case of the buoyancy flux, Φ_z, this implies rotationally advected fluid displaced significantly from its equilibrium position, which has not established a heavy over light configuration. In addition, the APE per unit volume of overturning regions is nearly double that of the non-overturning part of the flow. Thus, locally, the rotational
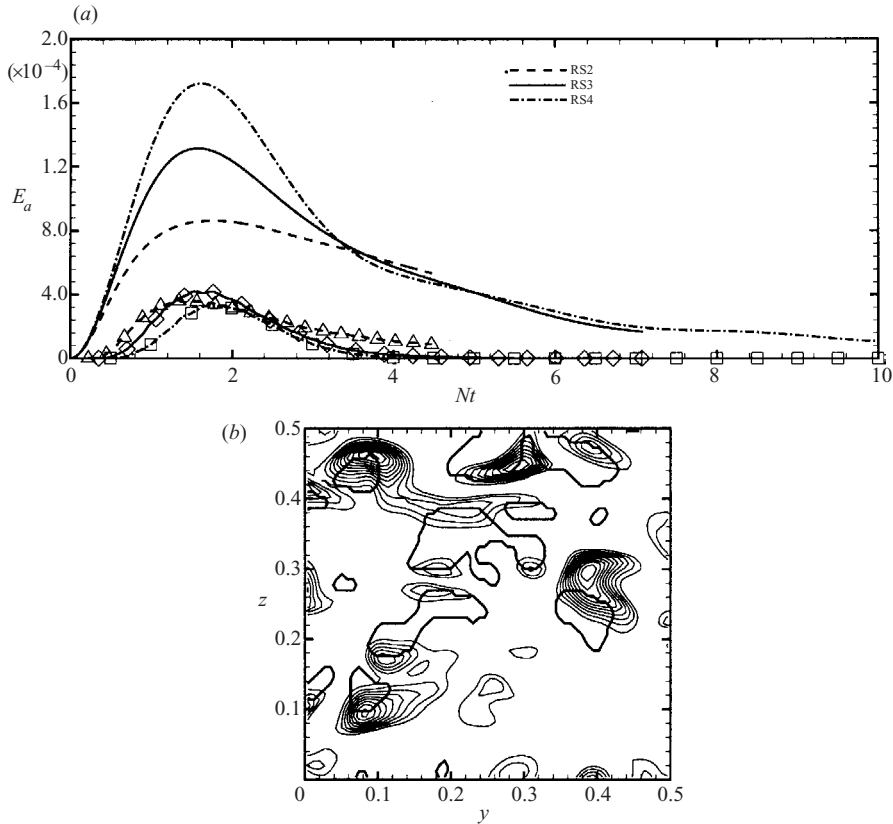
FIGURE 14. As figure 10 but for APE. (*b*) Overturn boundaries (thick solid lines) and contours of local value of APE normalized by its spatial average (solid line). Contour values are in the range [5, 35] with separation 3.

motion associated with overturning motion is more effective in generating high APE than non-overturning motions.

Finally, figure 15 shows the behaviour of the total diapycnal flux, $\Phi_d - \Phi_i$ (A 4). Evidently, diapycnal mixing is quite weak within the overturns, as would be expected from figures 4 and 9(*a*), which show that the strongest $\nabla\rho$ is associated with stable (negative) gradients and not unstable (positive) gradients which occur within overturns. This observation is consistent with those of KVA in their rake visualizations and reported negatively skewed pdf of $\partial\rho/\partial z$. Due to the restriction of their analysis to one-dimensional data and the Thorpe-sorted background profile, however, KVA were unable to quantify the contribution of overturning motions to the APE budget. In the DNS, the highest diapycnal flux within overturns occurs prior to the initiation of gravitational collapse ($Nt \approx 1.5$) and is responsible for the well-mixed interior of older overturns observed in figure 4 and serves as the basis of the collapsing lump model of Appendix B. However, figures 4 and 15(*b*) also indicate that the strongest $\nabla\rho$ and diapycnal flux, respectively, occur immediately outside and between adjacent overturning structures. This is due to the compressive strain occurring at the periphery of the high-rotation overturning motion. Thus, overturns appear to be crucial in terms of diapycnal mixing.
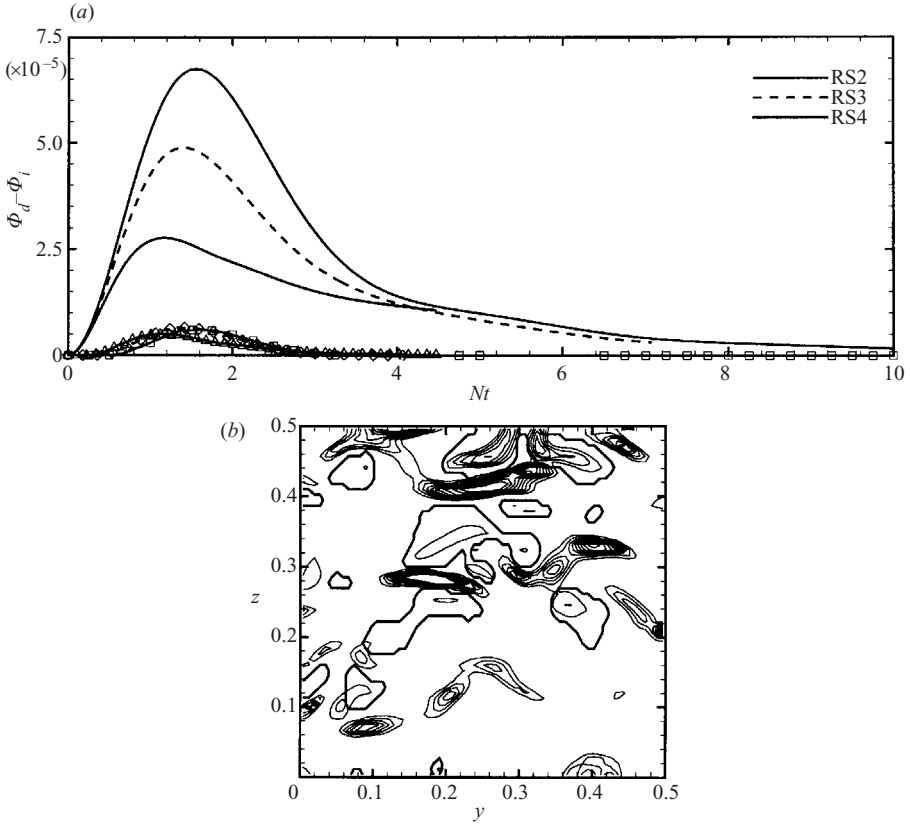
FIGURE 15. As figure 10 but for total diapycnal flux $\Phi_d - \Phi_i$. The quantity plotted for the overturns in (a) is specifically ($\int_{V_{OT}}(\nabla\rho)^2(-\mathrm{d}\rho/\mathrm{d}z_*)\mathrm{d}V - V_{OT}/L^3)$ $Ri/ScRe_L$), where V_{OT} is the volume occupied by the overturns. (b) Overturn boundaries (thick solid lines) and contours of local value of $(\nabla\rho)^2(-\mathrm{d}\rho/\mathrm{d}z_*)$ normalized by the mean density gradient (solid line). Contour values are in the range [2, 12] with separation 2.

A notable feature of the evolution of $\Phi_d - \Phi_i$ in all three runs is that it maintains a significant non-zero value at the same time that Φ_z goes to negligible values (for $Nt > 4$), i.e. diapycnal mixing still persists despite the suppression of overturning and turbulent mixing. KVA made a similar observation. They described their flow at this stage as a 'frozen' density field (i.e. near-static isopycnal surfaces) with localized high-$\nabla\rho$ regions void of any significant turbulent kinetic energy, which, however, are the cause of this non-negligible value of Φ_d. Further analysis may be required for runs of higher values of N to determine if these $\nabla\rho$ regions are the result of the interaction of out-of-phase internal wave modes, a greater range of which is supported by a higher buoyancy frequency. Finally, as discussed in Diamessis & Nomura (2000), $II \to 0$ at late times in buoyancy-dominated flows. Not only are high-rotation motions suppressed but so are localized high-strain flow patterns which would promote mixing of any horizontal inhomogeneities in the density field. Despite the non-negligible late stage Φ_d, the majority of the observed diapycnal mixing is caused by active turbulence and the associated overturning.

In summary, the interior of the overturns is not a major contributor to the quantities in the budgets of TKE and APE. However, this conclusion is contingent on the
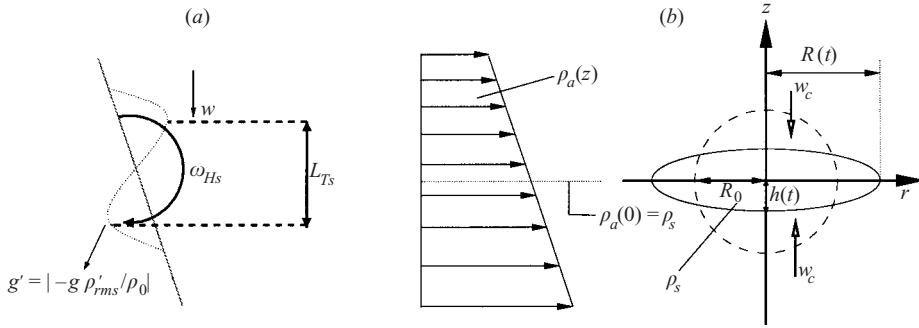
FIGURE 16. (*a*) A typical one-dimensional overturning segment (from Imberger 1994); w represents a typical collapse velocity and is used only for the purpose of illustration of the motion when buoyancy controls the overturn. (*b*) Model for the collapse of an initially well-mixed spherical fluid lump of initial radius R_0 in a linear ambient stratification (from Chen 1980). The lump exhibits a collapse which is radially symmetric in the horizontal while conserving its volume. The centre of mass of the lump is its equilibrium height.

definition of an overturn given in §3.1. Using this definition, overturn peripheries appear to be regions of significant energetic activity. If the energetic contribution of these boundary regions is included in characterizing the energetic significance of overturns (as is done in the field, where dissipation estimates are produced from averages computed over bins of a much larger vertical event than that of an overturning patch (Gregg & Sanford 1988), the overturns would indeed constitute regions of significant APE, buoyancy flux and diapycnal mixing.

5. Further analysis and discussion

5.1. *Activity diagrams of one-dimensional overturn segments*

The dynamics underlying the kinematic observations of §3.2 and §3.4 are now examined in greater detail. In the subsequent analysis, the local flow of an overturn is characterized to determine the relative significance of the turbulence versus the forces that tend to damp it out (viscous, diffusive, buoyancy etc.) and then mapped on a variant of the turbulent Froude number vs. turbulent Reynolds number activity diagram (see Imberger 1994, p. 152). In previous studies, the activity diagram has been used within a global framework, i.e. one point on the diagram describes an entire volume of turbulence (Ivey & Imberger 1991; Imberger & Ivey 1991; Saggio & Imberger 2001) under the assumption that point or vertical line measurements are representative of the global behaviour of the flow volume. In this work, the activity diagram is adapted to a local perspective with each point effectively representing a single overturning event. The distribution of points at any given time then provides information on the *population* of overturns in the flow. For the purpose of this analysis, each overturn is essentially characterized by an individual one-dimensional segment. This simplifies the analysis considerably while producing useful insight into the physical processes associated with overturns. The identification, isolation and tracking of three-dimensional overturn patches for the purpose of this analysis requires a complex algorithmic procedure and is a separate topic of ongoing investigation which is discussed elsewhere (Diamessis *et al.* 2002).

The analysis begins by establishing a simple conceptual model and characteristic quantities. Following Imberger (1994) and Saggio & Imberger (2001), consider a prototypical overturning segment, illustrated in figure 16(*a*). This segment consists

of a perturbation to a linear background stratification induced by one or more coherent vortices of strong resultant horizontal vorticity. One can then define: (*a*) a typical lengthscale, the r.m.s. Thorpe displacement, L_{Ts}, of the segment, (*b*) a typical horizontal vorticity (a quantity available in DNS data) along the segment, the r.m.s. value of fluctuating horizontal ω_{Hs} (the fluctuating component is used since stirring of the density field by the mean vorticity is countered by the mean strain (Diamessis & Nomura 2000), (*c*) a typical value for the reduced gravity, $g' = |-g\rho'_{rms}/\rho_0|$, where ρ'_{rms} is the r.m.s. of density fluctuations from the true background density gradient (not the local Thorpe-sorted density gradient) over the entire segment.

One may now define four characteristic timescales (see also Imberger 1994; Teoh, Ivey & Imberger 1997). The advective timescale, $t_a = \omega_{Hs}^{-1}$, is the time typical of the small-scale turbulence to stir the local density field by a length L_{Ts} (for the small scale-separation of the DNS, advection does occur primarily at small scales). The gravitational collapse timescale, $t_g = (L_{Ts}/g')^{1/2}$, is the time required for a fluid particle of reduced gravity g' in an overturning segment to return to its equilibrium position due to gravity. The viscous timescale, $t_v = L_{Ts}^2/\nu$, is the characteristic time for viscosity to decelerate any fluid motion induced by turbulence or buoyancy. The diffusive timescale, $t_d = L_{Ts}^2/D$, is the characteristic time for molecular diffusion to smooth any density perturbation across a segment of length L_{Ts}.

From the above definitions, the following three non-dimensional parameters are defined, which indicate the relative importance of these timescales within an overturning segment (critical values of these parameters are derived in Appendix B):

(*a*) Segment Froude number, Fr_S:

$$Fr_S = \frac{t_g}{t_a} = \left[\frac{L_{Ts}\,\omega_{Hs}^2}{g'}\right]^{1/2}. \tag{5.1}$$

Below the critical value $Fr_S < Fr_S^{cr} = 3.9$ (see Appendix B), the local small-scale turbulence cannot strain and mix and, in the present low-Re_λ DNS, overturn the density field against the restoring effect of gravity.

(*b*) Segment Reynolds number, Re_S:

$$Re_S = \frac{t_v}{t_a} = \frac{L_{Ts}^2\,\omega_{Hs}}{\nu}. \tag{5.2}$$

Using the same dissipation-range scaling as in Appendix B, we can write

$$Re_S = \left[\frac{L_{Ts}}{L_K}\right]^2. \tag{5.3}$$

Thus, Re_S reflects the extent of vertical stirring induced in the patch with respect to the viscous scale. Any overturn exhibiting $Re_S < Re_S^{cr} = 25$ (Appendix B), has overturning and straining motion impeded by viscosity.

(*c*) Segment Grashof number, Gr_S:

$$Gr_S = \frac{t_v^2}{t_g^2} = \frac{L_{Ts}^3 g'}{\nu^2} = \left[\frac{Re_S}{Fr_S}\right]^2. \tag{5.4}$$

The Grashof number compares the time it takes the momentum within an overturn to diffuse due to viscosity to the time it takes the isopycnals to return to their original position due to gravity. In overturns with $Gr_S < Gr_S^{cr}$, viscosity strongly counteracts the isopycnal collapse. Based on theoretical considerations proposed by Chen (1980) a value of $Gr_S^{cr} \in [400, 1200]$ is derived in Appendix B for the $Fr = 0.58$ runs given

the observations of §3.2 and §3.4 and the simple conceptual model of figure 16(b). For these specific runs, knowledge of Gr_S^{cr} is essential in interpreting their late-time dynamics. Note that this value of Gr_S^{cr} is dependent on the value of L_{Ts} at the beginning of gravitational collapse.

Activity diagrams using Fr_S and Re_S may now be generated. In order to represent the overturn population by a sample of one-dimensional segments, not all the profiles containing overturns in the sampled dataset are employed. The selected profiles are sampled at a separation distance at which the two-point xy correlation of the Thorpe displacement assumes a value of 0.2. Two profiles separated by this distance are essentially statistically independent as the overturning patterns in each one of them are sufficiently decorrelated. The separation distance in the x- and y-directions varied from 16 to 2 grid points, for the weakly and strongly stratified flows, respectively.

Figures 17 and 18 show activity diagrams corresponding to specific times for three runs: RUS1, RS1 and RS3. A significant range of values of Re_S and Fr_S is always observed. In all the runs, Re_S often lies below the critical value Re_S^{cr} as viscosity plays a significant role in the overturn dynamics due to the low Re_λ of our simulations. Note that the majority of events with $Re_S < Re_S^{cr}$ correspond to the smallest observed overturning scales. In run RS1 ($Ri = 0.05$), few points occur in the lower left quadrant, i.e. buoyancy has a negligible effect on all of the overturns (figure 17a). A significant number of overturns are dominated by inertial effects with $Re_S > Re_S^{cr}$, though viscosity remains important overall ($Re_S < Re_S^{cr}$ for the majority of points). Diffusion also plays a non-negligible role because $Pr = 0.7$ and the timescales of viscous and mass diffusion are comparable. Later in time (figure 17b), inertial effects remain significant with Re_S reaching as high as 300 for certain overturns. This trend continues throughout the duration of the simulation as the overturns, with the aid of the mean shear, grow through active turbulent stirring which remains uninhibited by buoyancy (figure 7a). Case RUS1 initially exhibits a similar trend (figure 17c). However, the turbulence has no source of energy to sustain it and is gradually damped out by viscosity (indicated by a reduction in Re_S in figure 17d). The size of the overturns initially grows similarly to case RS1, but eventually (time $Nt = 1.8$, see figure 7a) the overturns are large enough to be controlled by buoyancy and begin to collapse, as indicated by the majority of points characterized by $Fr_S \leqslant Fr_S^{cr}$ in figure 17(d).

When examining the dynamics of the patches in run RS3 ($Ri = 0.5$, figure 18a), one sees early on that inertial effects are still significant yet the influence of buoyancy is much stronger ($Fr_S < Fr_S^{cr}$). The inertial effects are rapidly overcome by buoyancy, as Re_S and Fr_S both decrease (figure 18b) along with the collapse in $\langle L_T \rangle$ (figure 7). Viscosity effectively counteracts buoyancy as shown by most points having $Gr_S < Gr_S^{cr}$, an effect of the low Re_λ of the DNS. Such a condition characterizes the viscous–buoyant state (VBS). However, by time $Nt = 4.24$ (figure 18c), inertial effects are almost negligible and nearly all the points on the diagram exhibit $Gr_S < Gr_S^{cr}$. Such an observation suggests that all remaining overturning motions have established a VBS (with overturns with $2L_{Ts} < 0.05$ upon collapse attaining a VBS at even lower Gr_S^{cr}) the initiation of which was predicted according to the lump model (Appendix B) to occur no later than $Nt \approx 2.3$. Beyond this point, according to the detailed similarity solution of Chen (1980), the overturn height drops very slowly with roughly a $t^{-1/5}$ power law, due to the retarding action of viscosity, which justifies the nearly constant value of $\langle L_T \rangle \approx 0.015$ in the final stage of flow evolution (figure 7a). If one calculates the non-dimensional value of t_d during this stage it is found that $t_d \approx \langle L_T \rangle^2 Re_L Pr/S \approx 3.66S^{-1} \to Nt_d \approx 2.58$ and is nearly equal to the duration of this
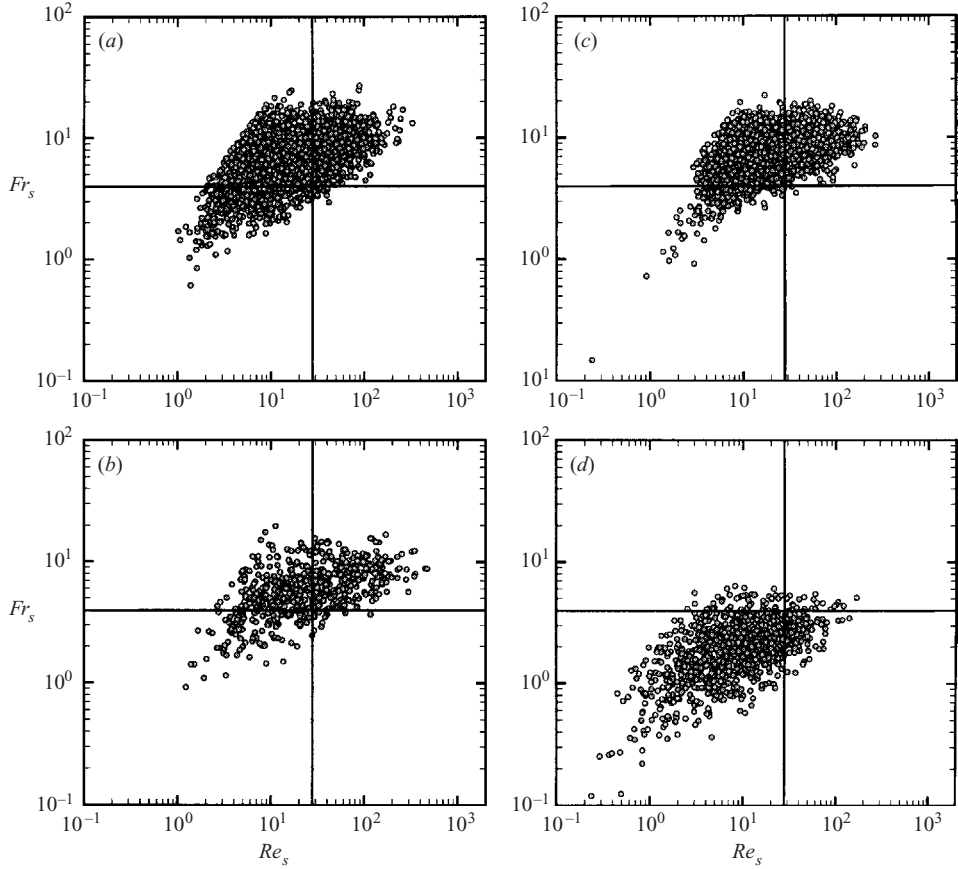
FIGURE 17. Activity (Fr_S vs. Re_S) diagrams of one-dimensional overturning segments. (*a*) Run RS1, time $Nt = 0.45$ ($St = 2$); (*b*) Run RS1, time $Nt = 1.8$ ($St = 8$); (*c*) Run RUS1, time $Nt = 0.45$; (*d*) Run RUS1, time $Nt = 1.8$. The critical values of Re_S and Fr_S are drawn on the diagrams. Each symbol on the activity diagrams represents a separate overturning segment in the vertical profiles sampled. See caption for figure 18 for apparent cut-off in the upper left quadrant.

interval of constant $\langle L_T \rangle$. Note that this constant $\langle L_T \rangle$ is evidently what KVA regard as a 'viscous cut-off' below which overturning cannot occur due to viscosity.

A scenario may now be constructed for the late stage of overturn evolution: gravitational collapse has been instigated at the larger scales of the internally well-mixed overturn which eventually attains a VBS (the occurrence time, t_{Bv}, and critical lengthscale, L_{Bv}, of which depend on the overturn height at the initiation of collapse) and the isopycnals are gradually locked in position (see Appendix B) so that the overturn maintains a constant vertical length. Owing to the small scales of these events, diffusion can act rapidly and homogenize their interior as they vanish into the ambient density field. The overturns that survive later than the others are likely to originate from larger initial patches with higher values of t_{Bv} and L_{Bv} as suggested by equation (B 3). The above analysis explains the observations made in §3.2 and §3.4 of the eventual drop in volume fraction of overturns, their relative constant vertical extent and the diffuse character of the density field within them. Similar behaviour was observed for the patch data of run RUS3, though the volume fraction of patches
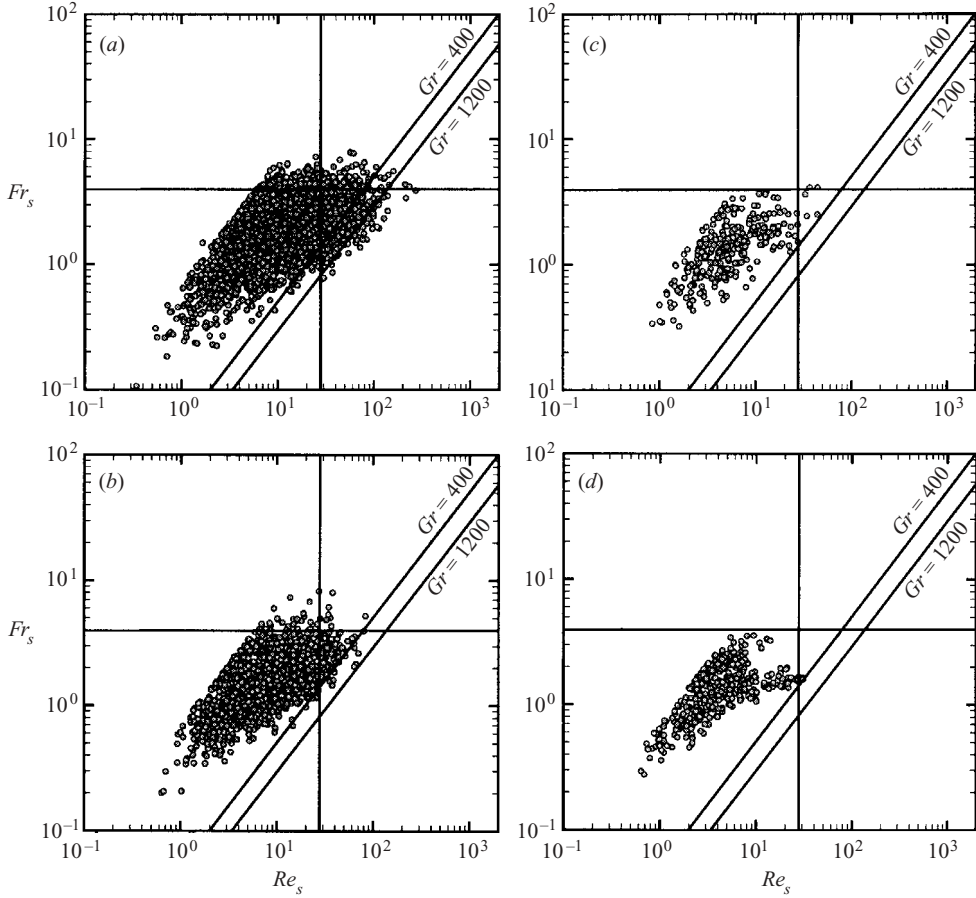
FIGURE 18. Activity (Fr_S vs. Re_S) diagrams of one-dimensional overturning segments. (*a*) Run RS3, time $Nt = 1.41$ ($St = 2$); (*b*) Run RS3, time $Nt = 2.82$ ($St = 4$); (*c*) Run RS3, time $Nt = 4.24$; ($St = 6$); (*d*) Run RS3, time $Nt = 5.68$ ($St = 8$). The critical values of Re_S and Fr_S are drawn on the diagrams. The lines $Gr_S = 400$ and 1200 denote the approximate interval of VBS establishment within an overturn. Each symbol on the activity diagrams represents a separate overturning segment in the vertical profiles sampled. The hard cut-off at $Gr \approx O(1)$ corresponds to the smallest overturns sampled, where $g' = N^2 L_{T_S}$ and Gr_S is simply a function of L_{T_S}.

diminishes much faster as the turbulence has no energy source (i.e. the mean shear) that would sustain it and allow the generation of a greater number of overturns. Note that run RUS1, despite the signs of some partial overturn collapse (figure 7*a*), is not characterized by a VBS phase before the end of the simulation, because t_{B_v} occurs much later due to the lower N and higher overturn height at the time of collapse instigation.

The skewness parameter of L_{T_S} (Teoh *et al.* 1997) was calculated for all overturn segment datasets considered in this section and was found to fluctuate in the range [0.9, 1.3]. Thus, L_{T_S} for all DNS overturn segments is moderately skewed toward values above its mean. However, the magnitude and variation of the skewness is significantly lower than those observed in the experiments of Teoh *et al.* (1997). There is also clearly no correlation between skewness and the distribution of points on the Re_S, Fr_S diagram.

As already mentioned, the use of dissipation-range scaling in the above analysis is valid because overturning is generated by dissipation-range coherent vortex tubes (see §4.1) and no inertial range is present due to the low Re_λ of the DNS. In the case of Re_λ high enough to be characterized by a prominent inertial range, dissipation-range scaling is not applicable. The largest overturns in the flow are then believed to be generated by the larger inertial-range scales of turbulence and inertial-range Kolmogorov scaling should be used in the definition of the advective timescale t_a. Fr_S and Re_S would then be equivalent to the turbulent Froude number, Fr_t, and Reynolds number, Re_t, respectively of Ivey & Imberger (1991).

The activity diagrams along with the analysis given in this section indicate that the overturn population at a given instant in the DNS data exhibits a fairly broad range of Re_S and Fr_S values, varying by up to two orders of magnitude (as in the energetic flow of RS1 in figure 17a), a range of values which can be even more extensive in higher-Re_λ flows (see Diamessis 2001, and §5.2). Thus, caution may be warranted when relying on information obtained from a single vertical measurement. The general trend of Re_S and Fr_S values is dictated by the stage of flow evolution and the values of Fr and Ri. Although viscosity is always non-negligible in this low-Re_λ DNS, the activity diagrams along with a collapsing well-mixed lump model provide a more complete description of the final phase of overturn evolution and clarify conjectures made by KVA (overturn size vs. number and the possibility of a viscous cut-off for overturning) with regard to this phase.

5.2. Higher-Re_λ behaviour

As noted in §2, computational limitations restricted this work to a relatively low value of initial Re_λ and Pr. Several questions arise. How does the DNS under consideration differ from existing DNS of higher Re_λ? Is it possible to use the DNS results to extrapolate the behaviour of stratified oceanic turbulence?

Results from DNS of stratified homogeneous sheared turbulence at the same resolution (128^3) obtained via a Fourier-spectral calculation, which allows greater accuracy and thereby initial $Re_\lambda \approx 90$ (Shih *et al.* 2000), have been analysed and are examined in greater detail elsewhere (Diamessis 2001). The analysis indicates qualitatively similar results with the present initial $Re_\lambda = 20$ dataset, the key difference being the slightly enhanced inertial force effects due to the more energetic initial turbulence (e.g. an increase in one order of magnitude in the observed maximum Re_S values). The absence of an inertial range, which may appreciably alter overturn dynamics, explains this qualitative similarity with an even higher Re_λ.

Regarding the second question, any attempt to extend the DNS results to oceanic turbulence should be made very cautiously as it is doubtful if the current DNS of stratified homogeneous turbulence of low Re_λ at $Pr = O(1)$ represents its oceanic counterpart for which maximum overturn lengthscales are of $O(1\,\text{m})$ or greater, $Re_\lambda \approx O(10^3)$ and $Pr \approx O(10^2)$. Although the VBS may correspond to Gibson's definition of fossil turbulence (Gibson 1991), because viscosity and buoyancy have dominated the overturn-generating inertial forces of the turbulence, it is highly unlikely that it will occur in the ocean because the overturn interior upon collapse would have a much less well-mixed interior than in the $Pr \approx O(1)$ case. One may also wonder if the overturn-generating dissipation-range vortical structures discussed in §4.1 are relevant in oceanic turbulence. For a flow with an inertial range of at least a couple of decades, conditions unattainable by current DNS, other overturn-inducing structures associated with these larger scales may be present. In the ocean, with the exception of highly energetic boundary regions, the energy spectra of observed overturns usually

exhibit a very limited inertial range (Gregg 1987). However, the dissipation-range characteristic vortex tubes are not likely to play a significant role in the dynamics of these overturns. Unlike the DNS with its limited range of scales, oceanic turbulence is still characterized by significant scale separation. A restricted or non-existent inertial range appears because low to moderate wavenumber activity is heavily influenced by buoyancy effects.

The picture of overturn dynamics at oceanic Re_λ remains far from complete. Although the recent stratified shear layer DNS by Smyth & Moum (2000) and Smyth *et al.* (2001) have provided invaluable insight into the dynamics of stratified turbulent overturns, their simulations touch upon only the lower end of the range of reported oceanic Re_λ. Once the necessary numerical/modelling methodologies and computational resources become available, the simulation of even higher-Re_λ stratified turbulence is imperative to investigate the delicate interplay between inertia and buoyancy in oceanic overturn dynamics throughout the different phases of their evolution.

6. Summary and conclusions

The structure and dynamics of overturns in stratified homogeneous turbulence are examined by utilizing full-field information from DNS. Here, overturns are defined through the density field as contiguous regions of non-zero Thorpe displacement. The effects of varying degrees of stratification and the presence of a background shear are considered. Although the DNS is limited to relatively low Reynolds number flows, the flow conditions (with shear) are comparable with those of KVA. Issues arising from the work of KVA are addressed and a more complete description in terms of the three-dimensional structure, dynamical evolution and energetic significance of overturns is developed. Results provide insight for the interpretation of physical measurements, typically limited to one-dimensional vertical profiles.

The three-dimensional structure of overturns is educed by extending the one-dimensional Thorpe method to three dimensions and visualizing contiguous regions with non-zero Thorpe displacement. The structure and its development are examined at the different phases of evolution. Overturns are initially generated by the stirring action of intense tube-like vortex structures which wrap the isopycnals around their cores thereby establishing gravitationally unstable regions. The overturns develop further through merging with adjacent overturns. During this growth phase, corresponding to increasing $\langle L_T \rangle$, overturns exhibit irregular spatial structure in unsheared flow and elongated structure with distinct orientation in shear flow. In the latter case, the preferential orientation of the vortex structures and associated prevalence of horizontal vorticity enhances the generation of overturns. This directional bias along with mean flow advection result in a distinct streamwise elongation and an orientation inclined from the horizontal in the corresponding overturns. These results elaborate on the description proposed by KVA which consisted of vertically advected lumps of fluid displacing localized stable temperature fronts. A collapse phase may follow the growth phase and occurs in the absence of sufficiently strong shear as buoyancy begins to control the larger scales of overturning motion. This phase is associated with decreasing $\langle L_T \rangle$. During the final phase of evolution, consistent with KVA's findings, $\langle L_T \rangle$ does not rapidly drop to zero but maintains a constant value for some period of time after the onset of collapse, as the number of overturns becomes progressively smaller. The overturns eventually vanish due to homogenization of their internal density distribution by diffusion.

The contribution of overturns to the energetics is determined through conditional statistics and direct inspection of visualizations of overturns and quantities associated with the turbulent kinetic energy (TKE) and available potential energy (APE) budgets. In general, the interiors of overturns are not, directly, a major contributor to the overall TKE and APE budgets of the flow. Results show that most of the APE in the flow comes from non-overturn (gravitationally stable) regions. It is found that the levels of TKE, turbulence production, buoyancy flux, and TKE dissipation rates in the overturn interiors scale with their volume fraction. Further investigation would be required for a more quantitative evaluation of the contributions of overturns versus that of non-overturn regions, with respect to the above quantities. However, the levels of APE in the overturn interior and periphery are signficantly higher than in the rest of the flow. In addition, strong buoyancy flux and the highest diapycnal mixing occur at the overturn peripheries. Overturns may therefore be considered active sites for stirring and mixing. This observation is especially evident during the growth phase when young overturns are being established. The stirring motion of the underlying vortex structures establishes high strain regions which amplifies local density gradients. Furthermore, the rotational motion is effective in establishing high APE. High TKE dissipation rates do not occur in overturns because they are associated with non-overturning vortex sheets. During the collapse phase, the energetic significance of overturns diminishes although high APE and diapycnal flux are still observed at the overturn peripheries. The overturn interiors appear to make a negligible contribution to negative buoyancy flux associated with restratification. At the late stage of evolution in which $\langle L_T \rangle$ attains a constant value, the energetic contribution of overturns is negligible. Some weak diapycnal mixing occurs in the 'frozen' isopycnal perturbations in non-overturning parts of the flow. However, without turbulent overturning and the associated stirring and straining, strong diapycnal mixing does not occur.

Further analysis is performed using activity diagrams to identify the prevalent dynamical processes in the overturn population. In this case, the data are examined in terms of one-dimensional profiles and the corresponding overturn segments. Activity diagrams sampled at different phases of flow evolution indicate a fairly broad range of overturn segment Reynolds and Froude numbers. Such a wide spread of values corroborates the need for multiple vertical profiling of a turbulent event to ensure representative sampling. The relatively low overturn segment Reynolds numbers illustrate the significant role of viscosity in these low Reynolds number simulations. The dynamics of the final phase of overturn evolution are described by a model for an axisymmetrically collapsing well-mixed lump of fluid which suggests that the collapsing overturn gradually attains a critical Grashof number and thus a viscous–buoyant state (VBS), thus explaining the observations of late-time constant $\langle L_T \rangle$. Diffusion-induced velocities operate on a timescale comparable to the duration of the VBS phase and act to annihilate all remaining overturns through homogenization of their internal density field.

Appendix A. Non-dimensional energy budget equations

In this section, the evolution equations for the turbulent kinetic energy (TKE) and available potential energy (APE) in a stably stratified homogeneous turbulent flow are presented. All primed quantities denote their fluctuating component with respect to the corresponding spatial mean values. Non-dimensionalization is performed using the reference values given in §2.

The TKE, denoted by E_k, of a fluid volume V is defined as

$$E_k = 0.5 \int_V (u'^2 + v'^2 + w'^2) \, dV. \tag{A 1}$$

The general evolution equation of the TKE is given in Winters *et al.* (1995). For the case of stably stratified homogeneous turbulence, it can be written in non-dimensional form as

$$\frac{dE_k}{dt} = \underbrace{-S \int_V u'w' \, dV}_{P} \underbrace{- Ri \int_V w'\rho' \, dV}_{\Phi_z} \underbrace{- \frac{1}{Re_L} \int_V \frac{\partial u_i'}{\partial x_k} \frac{\partial u_i'}{\partial x_k} \, dV}_{\varepsilon}, \tag{A 2}$$

where the term P is the production of TKE through the mean shear, Φ_z is the buoyancy flux and ε the integral of the TKE dissipation rate over the fluid volume V (written in tensor notation for brevity).

The APE, E_a, of the flow is the fraction of its total potential energy available for conversion to kinetic energy. The APE of a fluid volume V is defined in non-dimensional form as

$$E_a = Ri \int_V \rho \cdot (z - z_*) \, dV, \tag{A 3}$$

where z_* is the position of a fluid parcel in the background state of potential energy (BSPE), the state of minimum potential energy attained by the fluid at a given instant if allowed to restratify adiabatically (Winters *et al.* 1995; Winters & D'Asaro 1996; Peltier & Caulfield 2003). The total potential energy is thus the sum of the APE and the background potential energy associated with the BSPE. The general form of the APE budget can be found in Winters *et al.* (1995). For the case of stably stratified homogeneous turbulence, the non-dimensional representation is

$$\frac{dE_a}{dt} = \underbrace{Ri \int_V w'\rho' \, dV}_{\Phi_z} \underbrace{- \frac{Ri}{Sc \, Re_L} \int_V (\nabla\rho)^2 (-d\rho/dz_*)^{-1} \, dV}_{\Phi_d} + \underbrace{\frac{Ri}{Sc \, Re_L}}_{\Phi_i}, \tag{A 4}$$

where Φ_z has already been defined, Φ_d is the diapycnal flux and Φ_i the mean molecular flux of mass across V, which is constant for a linear mean density gradient. Φ_d represents the irreversible loss of APE due to molecular mixing across isopycnal surfaces (Winters & D'Asaro 1996).

For a numerical simulation dataset the BSPE can be obtained either through volume-sorting the density field (Winters *et al.* 1995) or from the p.d.f. of the density (Tseng & Ferziger 2001). In the case of DNS of homogeneous stratified

turbulence where $\mathrm{d}\bar{\rho}/\mathrm{d}z$ is fixed in time, the BSPE remains unchanged and equal to the value corresponding to initial mean uniform stable density stratification. In field observations or experimental data, a limited set of vertical density profiles is available. One then has to separately re-sort each of the individual profiles to obtain an estimate of the BSPE (Thorpe 1977; Dillon 1984; Itsweire *et al.* 1993; Winters & D'Asaro 1996).

Appendix B. Critical values of the segment non-dimensional parameters

In this section, critical values are derived for the non-dimensional parameters of an overturn segment used in §5.1, where the regimes of behaviour above and below each critical value are discussed in greater detail.

Segment Froude number, Fr_S: In the low-Re_λ regime, overturning is driven by small-scale dissipation-range coherent vortex tubes (see §4.1). Dissipation-range scaling may then be used for ω_{Hs} (defined in §5.1) within an overturning segment:

$$\omega_{Hs} \approx (\varepsilon_s/\nu)^{1/2}, \tag{B 1}$$

where ε_s is the dissipation rate averaged over the length of the segment. Thus, small-scale turbulence overturns and strains the density field over the same timescale. Through equation (B 1) and $t_g \approx N^{-1}$, Fr_S can be related to the small-scale Froude number, Fr_γ, of Ivey & Imberger (1991) and Imberger (1994),

$$Fr_S \approx \left[\frac{\varepsilon_s}{\nu N^2} \right]^{1/2} = Fr_\gamma . \tag{B 2}$$

Note that for all the DNS datasets, $Fr_S \approx Fr_\gamma$ is satisfied to an excellent degree. A critical value of $Fr_\gamma^{cr} = 3.9$ was obtained by Ivey & Imberger (1991) for the experimental observations of Stillinger *et al.* (1983), Itsweire *et al.* (1986) and Rohr *et al.* (1988). Thus, the critical value for Fr_S is $Fr_S^{cr} = 3.9$.

Segment Reynolds number, Re_S: Because overturning in the DNS is driven by dissipation-range coherent structures (se §4.1), it is reasonable to speculate that the process of an overturning motion overcoming viscosity is analogous to that of a small-scale motion overcoming the confines of the viscous boundary layer. To overcome viscosity in the boundary layer, any small-scale motion must exhibit a velocity $u \geqslant 5u^*$ and lengthscale $\mathcal{L} \geqslant 5L^*$ where u^* and L^* are the friction velocity and viscous scale, respectively (Kundu 2002), both of which can be shown to be approximately equal to the corresponding Kolmogorov scales. Thus, a critical value of $Re_S^{cr} = u\mathcal{L}/\nu = 25$ is readily obtained and used to characterize overturn segment dynamics.

Segment Grashof number, Gr_S: A critical value of Gr_S^{cr} may be determined by considering a simple conceptual model proposed by Chen (1980) and some of the kinematic observations made in §3.2 and §3.4. Using an analysis similar to but more detailed than Huppert (1982) (who only considered a homogeneous background density field for a viscous gravity current), Chen (1980) investigated theoretically and experimentally the instantaneous release of a volume-conserving immiscible well-mixed lump of fluid in a linear stratification for a variety of initial lump geometries. Figure 5(*a*) shows a typical late-time overturning region with a well-mixed interior which is most likely to have originated from the collapse of a larger, non-turbulent, fairly well-mixed overturn (such as the one located at $(y, z) = (0.25, 0.35)$ in figure 4*b*). One is thus motivated to apply Chen's analysis results to the DNS data. It is not unreasonable to then consider the *collapsing* overturns to initially have the idealized topology of well-mixed spherical lumps (figure 16*b*) undergoing an axisymmetric

collapse. Such an assumption should be acceptable even for the DNS flow with *uniform* background shear, as the linear $U(z)$ profile (not subject to instabilities) and the weak turbulence during collapse prevent the shear from making any significant dynamical contribution to overturn evolution. The shear simply has a geometric effect by deforming the collapsing overturn. However, in overturn boundary animations (not shown), no extreme patch distortions were observed (such as to cause splitting or shredding of a patch) during collapse that would invalidate use of the collapsing lump model. The initial spherical lump geometry is the most general choice, and although more complex geometries are discussed in Chen (1980), they are outside the scope of this work. To allow the direct substitution of the data of figure 7(*a*), non-dimensional equations (according to the non-dimensionalization of §2) in terms of Ri and Re_L are used. In the DNS simulations, the computational-domain Reynolds number, $Re_L = \Delta U L/\nu$ (or UL/ν) is equal to 23 256. In the following, when considering the unsheared runs, Ri should be replaced with $(NL/U)^2$. According to Chen (1980), the lump collapse is initially dominated by inertia/buoyancy and gradually transitions into a state where buoyancy is countered by viscosity to an increasing degree (which is manifested in the locking of isopycnal surfaces discussed in §5.1). This viscous–buoyant state (VBS) occurs at a time $t_{B\nu}$ after initiation of collapse, at a lump horizontal radius $R_{B\nu}$ and height $L_{B\nu} = 2h_{B\nu}$ given by

$$t_{B\nu} \approx \alpha_t \left[\frac{V_0^2 Re_L^3}{Ri^2}\right]^{1/7}, \quad R_{B\nu} \approx \alpha_R \left(V_0^3 Ri^{1/2} Re_L\right)^{1/7}, \quad L_{B\nu} \approx \frac{3}{2\pi\alpha_R^2}\left[\frac{V_0}{Ri\,Re_L^2}\right]^{1/7} \quad \text{(B 3)}$$

respectively, where $V_0 = 4\pi R_0^3/3$ is the initial volume of the lump and $\alpha_t = 0.0469$ and $\alpha_R = 0.407$. The height of the lump, $L_{B\nu}$, is calculated assuming it remains an ellipsoid with uniform horizontal radius $R_{B\nu}$ throughout the collapse and conserves its volume. For runs RS3 and RUS3, collapse begins at $Nt_c \approx 2$ (figure 7a). Diamessis (2001) shows that the height of a three-dimensional overturning patch upon onset of collapse at $Fr = 0.58$ is equal to its average Thorpe scale multiplied by a factor of approximately 2. Consequently, at $Nt_c \approx 2$ with $\langle L_T \rangle \approx 0.025$ (figure 7a), the average initial lump height can be assumed to be $L_0 = 2R_0 \approx 0.05$. For such a value of L_0 one can calculate $t_{B\nu}$ and show that the VBS begins at times $N(t_c + t_{B\nu}) \approx 2.3$. The rapid appearance of the VBS in the collapse process can be justified by the small vertical scale of the overturns (less than 1 cm high when dimensionalized according to the KVA data, which was restricted to the central 15 cm of their wind tunnel). Using the last of equations (B 3), the value of L_0 indicated above and $g' \approx N^2 L$ one finds that $Gr_S^{cr} \approx 1200$ upon the onset of the VBS. Note that this Gr_S^{cr} is dependent on the value of L_0. An overturn with L_0 half the above value exhibits $Gr_S^{cr} \approx 400$. Thus, the L_0-dependent Gr_S^{cr} is likely to fall in the interval $[400, 1200]$.

The above critical Gr may be constrasted to the critical values obtained by Barry (2002) for different DNS and experimental data. The latter span a range of values from 2 to 2×10^5 but describe a totally different phenomenon, that of a turbulent overturn in which the turbulence operates in such a way that the viscous diffusion timescale of momentum within the overturn is kept proportionate to the corresponding large-eddy turnover time. In contrast, the $Gr_S^{cr} \in [400, 1200]$ of this study describes locally a laminar flow at the final stages of overturn evolution.

REFERENCES

Barry, M. E. 2002 Mixing in stratified turbulence. PhD Dissertation, Dept. of Environmental Engineering, U. Western Australia.

CHEN, J. C. 1980 Studies on gravitational spreading currents. *Tech. Rep.* KH-R-40. California Institute of Technology, Pasadena.

DIAMESSIS, P. J. 2001 An investigation of vortical structures and density overturns in stably stratified homogeneous turbulence by means of direct numerical simulation. PhD Dissertation, University of California, San Diego.

DIAMESSIS, P. J., KERNEY, W. R., BADEN, S. B. & NOMURA, K. K. 2002 Automated tracking of 3-d overturn patches in direct numerical simulations of stratified turbulence. In *Applied Parallel Computing, 6th Intl Conf, Helsinki, Finland* (ed. J. Fagerholm). Lecture Notes in Computer Science, vol. 2367, pp. 557–566. Springer.

DIAMESSIS, P. J. & NOMURA, K. K. 1999 Interaction of vorticity, rate of strain, and scalar gradient in stably stratified homogeneous sheared turbulence. In *Turbulence and Shear Flow Phenomena – First Intl Symposium, Santa Barbara, California*, pp. 715–720.

DIAMESSIS, P. J. & NOMURA, K. K. 2000 Interaction of vorticity, rate-of-strain and scalar gradient in stratified homogeneous sheared turbulence. *Phys. Fluids* **12**, 1166–1188.

DILLON, T. M. 1982 Vertical overturns: A comparison of thorpe and ozmidov length scales. *J. Geophys. Res.* **87**, 9601–9613.

DILLON, T. M. 1984 The energetics of overturning structures: Implications for the theory of fossil turbulence. *J. Phys. Oceanogr.* **14**, 541–549.

DOMMERMUTH, D. G., ROTTMAN, J. W., INNIS, G. E. & NOVIKOV, E. A. 2002 Numerical simulation of the wake of a towed sphere in a weakly stratified fluid. *J. Fluid Mech.* **473**, 83–101.

GERZ, T., HOWELL, J. & MAHRT, L. 1994 Vortex structures and microfronts. *Phys. Fluids* **6**, 1242–1251.

GERZ, T. & SCHUMANN, U. 1989a In *Finite Approximations in Fluid Mechanics, Part 2* (ed. E. Hirschel) pp. 142–155. Vieweg.

GERZ, T. & SCHUMANN, U. 1989b Length scales of sheared and unsheared stratified homogeneous turbulence deduced from direct simulations. In *Seventh Symp. on Turbulent Shear Flows, Stanford, USA*.

GERZ, T., SCHUMANN, U. & ELGHOBASHI, S. 1989 Direct simulation of stably stratified homogeneous turbulent shear flows. *J. Fluid Mech.* **200**, 563–594.

GIBSON, C. H. 1980 Fossil temperature, salinity and vorticity in the ocean. In *Marine Turbulence* (ed. J. C. T. Nihoul), pp. 221–258. Elsevier.

GIBSON, C. H. 1986 Internal waves, fossil turbulence and composite ocean microstructure spectra. *J. Fluid Mech.* **168**, 89–117.

GIBSON, C. H. 1991 Laboratory, numerical and oceanic fossil turbulence in rotating and stratified flows. *J. Geophys. Res.* **96**, 12549–12566.

GIBSON, C. H., ASHURST, W. T. & KERSTEIN, A. R. 1988 Mixing of strongly diffusive passive scalars like temperature by turbulence. *J. Fluid Mech.* **194**, 261.

GREGG, M. C. 1987 Diapycnal mixing in the thermocline. *J. Geophys. Res.* **92**, 5249–5286.

GREGG, M. C. & SANFORD, T. B. 1988 The dependence of turbulent dissipation on stratification in a diffusively stable thermocline. *J. Geophys. Res.* **93**, 12381–12392.

HEBERT, D., MOUM, J. N., PAULSON, C. A. & CALDWELL, D. R. 1992 Turbulence and internal waves at the equator, part ii: Details of a single event. *J. Phys. Oceanogr.* **22**, 1346–1356.

HOLT, S. E., KOSEFF, J. R. & FERZIGER, J. H. 1992 A numerical study of the evolution and structure of homogeneous stably stratified sheared turbulence. *J. Fluid Mech.* **237**, 499–539.

HUPPERT, H. E. 1982 The propagation of two-dimensional and axisymmetric viscous gravity currents over a rigid horizontal surface. *J. Fluid Mech.* **121**, 43–58.

IMBERGER, J. 1994 Transport processes in lakes: review. In *Limnology Now: A Paradigm of Planetary Problems* (ed. R. Margalef), pp. 99–193. Elsevier.

IMBERGER, J. & IVEY, G. N. 1991 On the nature of turbulence in a stratified fluid. Part II: Application to lakes. *J. Phys. Oceanogr.* **21**, 659–680.

ITSWEIRE, E. 1984 Measurements of vertical overturns in a stably stratified flow. *Phys. Fluids* **27**, 764–766.

ITSWEIRE, E., HELLAND, K. & VAN ATTA, C. 1986 The evolution of grid-generated turbulence in a stably stratified fluid. *J. Fluid Mech.* **162**, 299–338.

ITSWEIRE, E., KOSEFF, J., BRIGGS, D. & FERZIGER, J. H. 1993 Turbulence in stratified shear flows: Implications for interpreting shear-induced mixing in the ocean. *J. Phys. Oceanogr.* **23**, 1508–1522.

IVEY, G. N. & IMBERGER, J. 1991 On the nature of turbulence in a stratified fluid. Part I: The energetics of mixing. *J. Phys. Oceanogr.* **21**, 650–658.

JACOBITZ, F. & SARKAR, S. 1999 On the shear number effect in stratified shear flow. *Theor. Comput. Fluid Dyn.* **13**, 171–188.

JACOBITZ, F., SARKAR, S. & VAN ATTA, C. 1997 Direct numerical simulations of the turbulence evolution in a uniformly sheared and stably stratified flow. *J. Fluid Mech.* **342**, 231–261.

KELLER, K. H. & VAN ATTA, C. W. 2000 An experimental investigation into the vertical temperature structure of homogeneous stratified shear turbulence. *J. Fluid Mech.* **425**, 1–29 (referred to herein as KVA).

KUNDU, P. K. 2002 *Fluid Mechanics*. Academic.

METAIS, O. & HERRING, J. R. 1989 Numerical simulations of freely evolving turbulence. *J. Fluid Mech.* **202**, 117–148.

MOUM, J. N. 1996 Energy-containing scales of turbulence in the ocean thermocline. *J. Geophys. Res.* **101**, 14095–14109.

NOMURA, K. K. & DIAMESSIS, P. J. 2000 The interaction of vorticity and rate of strain in homogeneous sheared turbulence. *Phys. Fluids* **12**, 846–64.

NOMURA, K. K. & ELGHOBASHI, S. E. 1992 Mixing characteristics of an inhomogeneous scalar in isotropic and homogeneous sheared turbulence. *Phys. Fluids* A **4**, 606–625.

NOMURA, K. K. & POST, G. K. 1998 The structure and dynamics of vorticity and rate of strain in incompressible homogeneous turbulence. *J. Fluid Mech.* **377**, 65–97.

PELTIER, W. R. & CAULFIELD, C. P. 2003 Mixing efficiency in stratified shear flows. *Annu. Rev. Fluid Mech.* **35**, 135–167.

POPE, S. B. 2000 *Turbulent Flows*. Cambridge University Press.

RILEY, J. J., METCALF, R. W. & WEISSMAN, M. A. 1981 Direct numerical simulations of turbulence in homogeneously stratified fluids. In *Non-linear Properties of Internal Waves*, pp. 79–112. AIP.

ROHR, J. J., ITSWEIRE, E. C., HELLAND, K. N. & VAN ATTA, C. W. 1988 Growth and decay of turbulence in a stably stratified shear flow. *J. Fluid Mech.* **195**, 77–111.

SAGGIO, A. & IMBERGER, J. 2001 Mixing and turbulent fluxes in the metalimnion of a stratified lake. *Limnol. Oceanogr.* **46**, 392–409.

SHIH, L. H., KOSEFF, J. R., FERZIGER, J. H. & REHMANN, C. R. 2000 Scaling and parameterization of stratified homogeneous turbulent shear flow. *J. Fluid Mech.* **412**, 1–20.

SMYTH, W. D. & MOUM, J. N. 2000 Length scales of turbulence in stably stratified mixing layers. *Phys. Fluids* **12**, 1327–1342.

SMYTH, W. D., MOUM, J. N. & CALDWELL, D. R. 2001 The efficiency of mixing in turbulent patches: inferences from direct simulations and microstructure observations. *J. Phys. Oceanogr.* **31**, 1969–1992.

STILLINGER, D. C., HELLAND, K. H. & VAN ATTA, C. W. 1983 Experiments on the transition of homogeneous turbulence to internal waves in a stratified fluid. *J. Fluid Mech.* **131**, 91–122.

TEOH, S. G., IVEY, G. N. & IMBERGER, J. 1997 Laboratory study of the interaction between two internal wave rays. *J. Fluid Mech.* **336**, 91–122.

THORPE, S. A. 1977 Turbulence and mixing in a scottish loch. *Phil. Trans. R. Soc. Lond.* A **286**, 125–181.

TSENG, Y. H. & FERZIGER, J. H. 2001 Mixing and available potential energy in stratified flows. *Phys. Fluids* **13**, 1281–1293.

WINTERS, K. B. & D'ASARO, E. A. 1996 Diascalar flux and the rate of fluid mixing. *J. Fluid Mech.* **317**, 179–193.

WINTERS, K. B., LOMBARD, P. N., RILEY, J. J. & D'ASARO, E. A. 1995 Available potential energy and mixing in density stratified fluids. *J. Fluid Mech.* **289**, 115–128.